REINFORCING EFFECT OF GRAPHENE OXIDE ON CEMENT MORTAR UNDER HIGH STRAIN RATE LOADINGS

BY

CHENYANG LI
BEng

A thesis submitted in fulfilment of the requirement for the degree of Master of Engineering Science (Research)

Department of Civil Engineering
Monash University
Clayton, Victoria 3800, Australia

March 2016

Copyright Notice

© The author 2016. Except as provided in the Copyright Act 1968, this thesis may not be reproduced in any form without the written permission of the author.

ABSTRACT

Reinforcing cement-based materials by nanomaterials has attracted extensive attention over the past decades. It has been reported that the mechanical properties of cement-based materials can be greatly improved by incorporating a small amount of nanomaterials. However, experimental and theoretical works have all focused on the enhancement of cement-based materials subjected to static loading. To the author's knowledge, no studies have reported on the mechanical properties of nanomaterial-reinforced cement-based composites under high strain rate loadings.

This study investigates the reinforcing effect of graphene oxide (GO) on cement mortar under high strain loadings. GO is an emerging nano-scale candidate for enhancing cement-based materials, which is valued for its two-dimensional geometry, superior mechanical properties and large surface area. Tensile splitting and compression tests were conducted on GO-reinforced cement mortar under both static and high strain rate loadings. The high strain rate testing was performed using a Split Hopkinson Pressure Bar (SHPB) apparatus. Static experiments showed that incorporation of GO (of 0.02 wt% of cement) improved the tensile splitting and compression strength of plain cement mortar by 8.9% and 10.8%, respectively, and there was little difference between the 0.02 wt% and 0.04 wt% GO addition. The SHPB tests showed that the reinforcing effect of GO under high strain rate is directly related to the number of cracks. In tensile splitting tests, because the major crack is always localized in the centre of the specimen regardless of the strain rate, the reinforcing effects of GO on cement mortar were the same for different strain rates. In compression tests, however, because the cracks were diffused and there were more cracks under high

strain rates, the reinforcing effect of GO was also more significant under higher strain rates.

To understand the reinforcing mechanisms of the nanomaterials, the key is to determine the interaction properties between the nano-scale reinforcements and the cement matrix. However, understanding of the governing forces in the reinforcement's pull-out behaviour at such a small scale is still very limited. The present study is the first to identify the governing force during the pull-out of atomically thin two dimensional (2D) nanosheets (e.g. graphene and its derivative GO) and to develop corresponding theoretical models. In molecular dynamic (MD) simulations, friction was found to make negligible contribution to the pull-out force because of the lack of asperities on atomically thin materials (ATM). The pull-out force was revealed to be governed by a "crack plane adhesion". Unlike frictional pull-out, crack plane adhesion produces a pull-out force independent of the embedded length of ATM. The magnitude of pull-out force and its affecting factors were investigated by MD simulations. On the basis of crack plane adhesion, the relation between the pull-out force and the pull-out displacement for ATMs was formulated. Furthermore, a new theoretical model was developed to predict the crack bridging stress (σ_B) of 2D ATMs. The magnitude of maximum σ_B was estimated to be 3MPa for 0.2 wt% of GO in cement matrix, which was used in the finite element simulations as discussed herein. The fundamental theory and new model proposed here serve as theoretical support for understanding and development of ATM-reinforced composite materials.

Finite element simulations for static and SHPB compression tests were conducted using a micromechanical model, the microplane model. First, the microplane model was examined by comparative study with the commonly used concrete damaged plasticity model. Then finite element simulation models of static and SHPB

compression tests were built in *ABAQUS*. For simulation of the static test, by including the calculated crack bridging stress into microplane model, the experimental compressive strength of GO-reinforced cement mortar could be accurately simulated, which validated the calculation of the crack bridging stress by the proposed model in Chapter 4 and the effectiveness of the microplane model to simulate the static behaviour of GO-reinforced cement-based composites. For simulation of the SHPB test, the microplane model with a logarithmic relation between the dynamic increase factor (DIF) and the strain rate to account for the strain rate effect worked for the simulations of plain cement mortar samples. However, for simulation of the GO-reinforced mortar samples, the simulation results give a significant underestimation compared with the experimental results under higher strain rates.

ABBREVIATIONS

ADB	Adhesion band
ATM	Atomically thin materials
CDP	Concrete damaged plasticity model
CNT	Carbon nanotube
C-S-H	Calcium silicate hydrate
DIF	Dynamic increase factor
EDS	Energy-dispersive xray spectroscopy
GO	Graphene oxide
IMLG	Isolated monolayer graphene
ITZ	Interfacial transition zone
MD	Molecular dynamics
MLG	Mono layer graphene
MWCNT	Multi-walled carbon nanotube
OPC	Ordinary Portland cement
SEM	Scanning electron microscope
SG	Strain gauge
SHPB	Split Hopkinson Pressure Bar
SWCNT	Single-walled carbon nanotube

DECLARATION

This thesis describes my research work carried out in the Department of Civil Engineering at Monash University in Australia during the candidature period from March 2014 to March 2016. The thesis is submitted to Monash University in total fulfilment of the requirements for the degree of Master of Engineering Science (Research).

The thesis contains no material which has been accepted for the award of any other degree or diploma in any university or institution and no material which has been previously written or published by another person except where due reference is made in the text of the thesis.

_____

Chenyang Li

March, 2016

ACKNOWLEDGEMENTS

Foremost, I would like to express my greatest gratitude to my main supervisor, Associate Professor Wenhui Duan. Without his sharing expertise, sincere guidance and insightful feedback, I would not have been able to accomplish this research program. I would also like to acknowledge the financial support provided by Monash University through the Monash Graduate Scholarship and the Faculty of Engineering International Research Scholarship scheme.

In addition, I am grateful to Associate Professor Dong Ruan, my co-supervisor Dr Ye Lu and my senior colleagues Dr Shujian Chen, Dr Xiangyu Li, Dr Asghar Habibnejad Korayem, Mr Kenan Feng and Mr Fujia Luo for their guidance and advice in my research work. Thanks are also due to the staff in the Civil Engineering Laboratory and Monash Centre for Electron Microscopy for their assistance in my experimental program. I must also acknowledge the Research and Postgraduate Manager of Civil Engineering Department, Mrs Jenny Mason, for her much appreciated help during the past two years.

Finally, I wish to dedicate this thesis to my parents (Mrs Linxia Jiang and Mr Yujun Li) and my girlfriend (Miss Suyuan Tian) for their great love, support and encouragement throughout my life.

LIST OF CANDIDATE'S PUBLICATIONS

REFEREED JOURNAL PAPERS

AH Korayem, **CY Li**, QH Zhang, XL Zhao, and WH Duan, "Effect of carbon nanotubes modified epoxy adhesive on CFRP-to-steel interface". *Composites Part B: Engineering*, 2015. 79(15): p. 95–104.

CY Li, X Li, D Ruan, and WH Duan, "Experimental Analysis of graphene oxide reinforced mortar composites subjected to static and high strain rate loadings", *under review*.

CY Li, SJ Chen, and WH Duan, "The governing forces in the pull-out of atomically thin materials", *under review*.

X Li, **CY Li**, YM Liu, SJ Chen, CM Wang, JG Sanjayan, and WH Duan, Improvement of mechanical properties by incorporating graphene oxide into cement mortar, *Mechanics of Advanced Materials and Structures*, Accepted on 8 March 2016

SJ Chen, Y Tian, **CY Li**, and WH Duan, A new scheme for analysis of pore characteristics using centrifuge driven non-toxic metal intrusion, *Geomechanics and Geophysics for Geo-energy and Geo-Resources*, Accepted on 20 March 2016

AH Korayem, SJ Chen, QH Zhang, **CY Li**, XL Zhao, and WH Duan, Failure of CFRP-to-steel double strap joint bonded using carbon nanotubes modified epoxy adhesive at moderately elevated temperatures, *Composites Part B: Engineering*, Accepted on 13 March 2016

X Li, AH Korayem, **CY Li**, YM Liu, HS He, JG Sanjayan and WH Duan, "Incorporation of graphene oxide and silica fume into cement paste: A study of dispersion and compressive strength", *under review*.

TABLE OF CONTENTS

ABSTRACT 2

ABBREVIATIONS ..... **iv**

DECLARATION ..... **v**

ACKNOWLEDGEMENTS ..... **vi**

LIST OF CANDIDATE'S PUBLICATIONS ..... **vii**

TABLE OF CONTENTS ..... **ix**

LIST OF FIGURES ..... **xii**

LIST OF TABLES ..... **xv**

CHAPTER 1. INTRODUCTION **1**

1.1. Background 1

1.2. Research Aim and Objectives 3

1.3. Structure of Thesis 4

CHAPTER 2. LITERATURE REVIEW **7**

2.1. Introduction 7

2.2. GO-reinforced Cement-Based Composites 7

2.3. Strain Rate Effect 10

2.3.1. Strain Rate Effect of Cement-Based Materials 10

2.3.2. High Strain Rate Test and Split Hopkinson Pressure Bar (SHPB) 13

2.4. Numerical Investigations 15

2.4.1. MD Simulations of Nanoscale Reinforcements 15

2.4.2. Crack Bridging Model for Fibre-Reinforced Cementitious Composites 16

2.4.3. Finite Element Simulations Using Microplane Model 17

2.5. Research Gaps 20

CHAPTER 3. EXPERIMENTAL RESULTS OF GO-REINFORCED CEMENT MOTAR UNDER STATIC AND HIGH STRAIN RATE LOADINGS 21

3.1. Introduction 21

3.2. Experimental Program 21

3.2.1. Materials 21

3.2.2. Mix Design and Mixing Procedure 23

3.2.3. Tests Quasi-static Splitting Tensile and Compression Tests 24

3.2.4. Setup and Data Processing of SHPB 24

3.3. Results and Discussion 26

3.3.1. GO Identification 26

3.3.2. Static Tests 27

3.3.3. Tensile Splitting and Compressive Strength under High Strain Rate Loadings 29

3.3.4. Analyses of Failure Modes and GO Reinforcing Effect under High Strain Rate 33

3.4. Conclusions 36

CHAPTER 4. MD SUMULATION AND A NEW CRACK BRIDGING MODEL FOR ATOMICALLY THIN MATERIALS REINFORCED COMPOSITES 37

4.1 Introduction 37

4.2 Simulation Methods 39

4.2.1 Simulation of Friction 39

4.2.2 Simulation of Pull-out 40

4.3 Pull-out at Atomic Scale 41

4.3.1 Validation of Friction Governed Pull-out 41

4.3.2 Governing Forces at Atomic Level: Crack Plane Adhesion 44

4.3.3 A New Model for the Reinforcing Effect of 2D ATM 48

4.4 Conclusions 52

CHAPTER 5. FINITE ELEMENT SIMULATIONS USING MICROPLANE MODEL 54

5.1 Introduction 54

5.2 Comparative Study of Microplane Model and Concrete Damaged Plasticity Model 55

5.2.1 Finite Element Model 55

5.2.2 Single Point Simulation for Parameters Calibration 57

5.2.3 Results and Discussion 59

5.3 Numerical Simulations of Static and SHPB Tests Using Microplane Model 61

5.3.1 Simulations of Static Compression Test 61

5.3.2 Simulations of SHPB Compression Test 64

5.4 Conclusions 67

CHAPTER 6. CONCLUSIONS AND RECOMMENDATIONS 69

6.1 Conclusions 69

6.2 Recommendations for Future Studies 70

APPENDIX A: DERIVATION OF CRACK PLANE ADHESION GOVERNED PULL-OUT LAW 72

APPENDIX B: DERIVATION OF CRACK BRIDGING STRESS 75

REFERENCES 77

LIST OF FIGURES

Figure 2.1 (a) Wrinkled graphene (Duan et al., 2011) and (b) graphene oxide (Bagri et al., 2010) 9

Figure 2.2 Effect of 0.05 wt.% GO: (a) Stress-strain curves under compression; (b) Load-displacement curves under flexure (Pan et al., 2013) 9

Figure 2.3 Variation of load-carrying capacity with strain rate for concrete in uniaxial compression (Cotsovos and Pavlović, 2008) 11

Figure 2.4 Best-fit curves of results obtained from uniaxial compression test (Cotsovos and Pavlović, 2008) 11

Figure 2.5 Strain rate regime and corresponding experimental techniques (Nemat-Nasser, 2000). 14

Figure 2.6 Typical SHPB test setup. Reproduced from Wu et al. (2010)..... 15

Figure 2.7 A fibre crossing a matrix crack plane (Li et al., 1991)..... 17

Figure 2.8 (a) Microplane strain vector; (b) microplane strain components. Reproduced from (Caner and Bažant, 2012) 18

Figure 3.1 SEM image of GO nanosheets (Li et al., 2016a)..... 22

Figure 3.2 Particle size distribution of sand (Li et al., 2016b) 23

Figure 3.3 SHPB set-up 26

Figure 3.4 SEM images of sand surface with GO 27

Figure 3.5 EDS spectra of point 1 (with GO) and point 2 (without GO) 27

Figure 3.6 Static tensile splitting strength 28

Figure 3.7 Static compressive strength..... 28

Figure 3.8 Tensile splitting strength under high strain rate 30

Figure 3.9 DIF of specimens under high strain rate tensile splitting tests..... 31

Figure 3.10 Compressive strength under high strain rate 32

Figure 3.11 DIF of specimens under high strain rate compression tests 33

Figure 3.12 Fragments of specimens under high strain rate tensile splitting loading..... 33

Figure 3.13 Fragments of specimens under high strain rate compression loading..... 34

Figure 3.14 SEM images of sand fragments under high strain rate loadings 34

Figure 3.15 Mass comparison after separation by a 3.5mm sieve 35

Figure 4.1. Schematics of a) friction governed micro-/nanofibre pull-out (red areas indicate friction-damaged materials during pull-out), and b) adhesion resistance for ATM during pull-out (circles/arcs indicate different force equilibrium at locations I, II and III)..... 42

Figure 4.2. (a) Snapshot of a sliding graphene in a periodic simulation box with PE matrix and the decrease of speed of due to friction in b) C-S-H (△), c) metal (○) and d) polymer (□) matrices. 43

Figure 4.3 Forces on atoms in IMLG in x direction F_x (c, f, h and j) and cumulative F_x (a, d, g and i) applied by the matrix when the IMLG is (a and c) half pull-out and (b and f) ¾ embedded in a C-S-H matrix (△) and half embedded in (g and h) Al (○) and (i and j) PE (□) matrix. (b) and (e) show snapshots of the MD model at the corresponding pull-out distances. 46

Figure 4.4 Snapshot of pull-out of a monolayer graphene from b) metallic (Al), c) polymeric (PE), and a) and d) cementitious matrices (C-S-H) and (e, g, i and k) $E_{p,ad}$ and (f, h, j and l) changing rate of $E_{p,ad}$ against δ for 20×20* Å (◇), 40×20 Å(✳), 60×20 Å(△), 40×40 Å(▷) graphene and 60×20 Å functionalised graphene (☆) pull-out from C-S-H matrix and 60×20 Å graphene pull-out from Al (○) and PE (□) matrix. Parts of the matrices in (a) and (d) are made invisible to show the embedded part of the graphene sheet. *the dimensions of the sheet are indicated as length × width, with length is in the pull-out direction. 48

Figure 4.5 a) pull-out model of a section of an ATM sheet with infinitesimal width, b) randomly oriented disk model in 3D space, c) demonstration of debonding and debonded parts during pull-out and d) σ_B vs δ where red, blue and green curves and arrows indicate the effect of increasing G_d, C and r respectively. 52

Figure 5.1 (a) geometry, loading and boundary conditions; (b) finite element mesh 56

Figure 5.2 Calibration of stress-strain relation under uniaxial tension and compression 58

Figure 5.3 Load versus displacement at point B with different models 60

Figure 5.4 Load versus displacement at point B with different element deletion criteria in M7 model..... 61

Figure 5.5 Finite element model of quasi-static compressive test 62

Figure 5.6 Crack bridging stress of GO-reinforced cement mortar 64

Figure 5.7 Finite element model of SHPB test 65

Figure 5.8 Simulation results of SHPB test 67

LIST OF TABLES

Table 3-1 Chemical compositions of cement powder 22

Table 3-2 Mix design of the mortar samples 24

Table 4-1. Decreasing rate of velocity and computed friction coefficient. 43

Table 5-1 Parameters of compressive and tensile behaviour in CDP model.....57

Table 5-2 Single-point simulation results under equibiaxial tension and compression 59

Table 5-3 Contact properties in the normal direction of the interfaces 64

CHAPTER 1. INTRODUCTION

1.1. Background

Cement is one of the most popular construction materials, widely used around the world. As a binder, cement is a major ingredient of cement-based materials (paste, mortar, concrete and composite concrete). However, structural applications of cement-based materials have been limited due to their poor resistance to crack formation, weak tensile strength and low strain capabilities (Neville and Brooks, 1987). On the other hand, the production of cement involves massive release of greenhouse gas into the atmosphere. Therefore, researchers have attempted different ways to improve the mechanical properties of cement-based materials, which can also reduce the amount of cement consumed and the emission of greenhouse gas.

Nano-modifying and reinforcing materials have demonstrated promising effects to improve the mechanical properties of cement-based materials (Sanchez and Sobolev, 2010). On the basis of the morphology of these nanomaterials they can be classified into three types: zero-dimensional (0D) nanoparticles (e.g. nanosilica), one-dimensional (1D) nanofibres (e.g. carbon nanotubes) and two-dimensional (2D) nanosheets (e.g. graphene and its derivative graphene oxide). Nanosilica is valued for its high chemical pozzolanic activity, nucleation effect and pore filling effect, which can densify the microstructure and the interfacial transition zone (ITZ) of cement-based composites (Sanchez and Sobolev, 2010, Singh et al., 2013). However, since 0D nanoparticles have a spherical shape and low aspect ratio, they lack a crack bridging effect. It has been reported that the inclusion of CNTs can improve the static mechanical properties of cement paste (Chen et al., 2011, Zou et al., 2015). However, the water

insolubility of CNTs results in poor dispersion in water (Chen et al., 2011, Chen et al., 2014), which limits its applications in reinforcing cement-based materials.

2D geometry graphene oxide (GO) can be a better alternative than CNTs for reinforcement of cement-based materials (Chuah et al., 2014), not only because it has a larger surface area for better bonding with the matrix, but because the oxygen-containing functional groups of GO sheets render them hydrophilic and highly dispersible in water (Qiu et al., 2010a). Current work has found that GO can improve the mechanical properties (compressive strength, flexural strength, etc.) of cement under static loadings (Gong et al., 2014, Pan et al., 2015). However, the dynamic responses of the composites and the reinforcing mechanism of GO are rarely investigated.

Understanding of the strain rate effect of cement-based materials is important for construction safety under impact and blast loads. It is generally accepted that the strength of cement-based materials will increase with the increase of strain rate. One major mechanism to explain the strain rate sensitivity of cement-based materials is the effect of micro-crack inertia (Tedesco et al., 1993). Correspondingly, it is expected that the inclusion of GO with crack bridging behaviour will have an effect on the dynamic mechanical properties of cement-based composites.

In this study, plain cement mortar samples and GO-reinforced cement mortar samples were fabricated and tested by tensile splitting and compression experiments under both static and high strain rate loadings. MD simulations were conducted and a new theoretical model was developed to describe the pull-out behaviour of 2D nanosheets to explain the reinforcing effect of GO and quantify the crack bridging stress. Finally, the calculated crack bridging stress was implemented into the microplane

model and finite element simulations for static and SHPB compression tests were conducted using the microplane model.

1.2. Research Aim and Objectives

Based on earlier research in Duan's group (Department of Civil Engineering at Monash University) with GO as the nano-reinforcement to improve the static mechanical properties of cement composites, this two-year Masters research project aimed to investigate the effect of high strain rate on the reinforcing effect and reinforcing mechanism of GO on cement mortar. Research in this area is essential for understanding the response of GO-reinforced cement-based materials under impact and blast loading. The following specific objectives were identified to achieve the research aims:

(1) To study the effect of strain rate on the mechanical properties of GO-reinforced cement mortar.

It is widely acknowledged that the dynamic strength of cement-based materials increases when they are subjected to high strain rate. Whether the inclusion of GO will affect the strain rate sensitivity of cement-based composites is still unknown. In this study, GO was dispersed in water using ultra-sonication and then incorporated into cement mortar with different concentrations (Pan et al., 2015). Both tensile splitting and compression tests were conducted for plain cement mortar and GO-reinforced cement mortar under static and high strain rate loadings. The static behaviour of the samples was characterized using a universal testing machine. The SHPB apparatus was adopted to test the mechanical properties under high strain rate loadings, as it can achieve strain rate at the range around 10-2000 s^{-1}. The fragments of the samples after SHPB testing were collected and analysed to study the strain rate effect of GO-reinforced cement mortar and the reinforcing effect of GO under high strain rate.

(2) To study the reinforcing mechanism of ATM such as GO

Although many researchers have reported that the incorporation of GO could improve the mechanical properties of different types of composites, no existing model to quantitatively describes the reinforcing effect of GO. In this study, MD simulation was used to investigate the pull-out behaviour of 2D ATM such as graphene and GO from different matrices. The results from the MD simulations were used to develop a crack bridging model for composites reinforced by 2D ATM. The calculated crack bridging stress was then adopted and validated in finite element simulations using the microplane model to simulate the static and SHPB compression tests.

1.3. Structure of Thesis

This thesis consists of six chapters, three of which are the main chapters (Chapters 3, 4 and 5), addressing respectively the experimental results of GO-reinforced cement mortar composites under static and high strain rate loadings, MD simulation and a new model for estimating the crack bridging stress of GO, and the finite element simulations using the microplane model. The introduction, literature review, and conclusion and recommendations are presented in Chapters 1, 2, and 6, respectively.

Chapter 1 introduces the background of GO-reinforced cement-based material and the importance of studying its behaviour under high strain rate. Then the research aim and objectives are clarified and thesis structure is outlined.

Chapter 2 first reviews the current state of knowledge of cement-based composites reinforced by nanomaterials, especially by GO. The strain rate effect of cement-based composites is discussed. Finally, a review of the numerical simulations in this study is presented.

Chapter 3 presents the experimental work on GO-reinforced cement mortar composites. Both tensile splitting and compression tests were conducted under static and high strain rate loadings. The high strain rate testing was performed using a SHPB apparatus. The effects of high strain rate on the tensile splitting and compressive strength of GO-reinforced cement mortar were presented in comparison with the plain cement mortar. The fragments of the samples after SHPB testing were collected to observe the failure mode. By analysing the experimental results and the failure mode, the reinforcing effect of GO under static and high strain rate loadings were explored and discussed.

Chapter 4 investigates the interactions between 2D ATM such as GO and different matrices. MD simulations were conducted to identify the governing force during the pull-out of these 2D ATM. A new theoretical model for composites reinforced by 2D ATM was developed, by which the crack bridging stress of GO-reinforced cement mortar could be estimated.

Chapter 5 presents the finite element simulations using the microplane model. First, the microplane model was examined by a comparative study between the microplane model and the widely used concrete damaged plasticity model. Then, finite element simulations were conducted to simulate the static and SHPB compression tests described in Chapter 3. The calculated crack bridging stress based on the model in Chapter 4 was used in the microplane model to model the behaviour of GO-reinforced cement mortar.

Chapter 6 summarizes the thesis with the main conclusions and presents recommendations for future research.

Appendices A and B present the detailed derivation of the equations for the crack plane adhesion governed pull-out law and crack bridging stress, respectively.

CHAPTER 2. LITERATURE REVIEW

2.1. Introduction

This thesis investigates the reinforcing effect of GO on cement mortar under high strain rate loadings. Correspondingly, the literature review begins with introduction of the materials investigated in this research, GO-reinforced cement-based composites. This is followed by an overview of the strain rate effect of cement-based materials and the typical high strain rate experimental testing method. In particular, the Split Hopkinson Pressure Bar (SHPB) is presented as the main testing technique. Finally, relevant background is presented regarding the numerical investigations in this study, namely the MD simulations of nanoscale reinforcement, the crack bridging model for fibre-reinforced cementitious composites and the finite element simulations using the microplane model.

2.2. GO-reinforced Cement-Based Composites

Poor resistance to crack formation, weak tensile strength and low strain capabilities are the key disadvantages of cement-based materials in modern construction (Neville and Brooks, 1987). To mitigate the weak tensile performance of cement-based materials, reinforcements are essential for cement-based materials used for structural purposes. apart from traditional steel reinforcements, the use of microfibres (steel, glass, synthetic and natural fibres) to reinforce cement-based materials has been extensively reported (Balaguru and Shah, 1992, Bentur and Mindess, 2006, Mehta, 1986). The inclusion of these microfibres with diameter of a few to tens of microns has increased the toughness and tensile strength of concrete and other cement-based materials by stabilizing microcracks.

However, these fibres have a relatively small surface area, which limits the interfacial strength between matrix and fibre (Wichmann et al., 2008) and they cannot prevent crack initiation at nanoscale (Chuah et al., 2014).

Nanoscale reinforcements such as carbon nanotubes (CNTs) have been found to be more efficient for improving the mechanical properties of cement-based materials. It has been reported that CNTs can decrease porosity and increase the crack bridging capacity of cement pastes at nanoscale and, with the addition of 0.075 wt% CNTs, the Young's modulus, flexural strength and fracture energy of cement pastes can be increased by 31.54%, 48.89% and 62.55%, respectively (Zou et al., 2015). However, the poor dispersion of water-insoluble CNTs has been a major challenge (Chen et al., 2011, Chen et al., 2014), which limits the application of CNTs in reinforcing cement-based materials.

The properties of 2D atomically thin nanosheet of graphene oxide (GO) have been found to be suitable to achieve higher reinforcing effect. As a graphene derivative, GO consists of a hexagonal carbon network bearing hydroxyl and epoxide functional groups on the basal planes, as well as carbonyl and carboxyl groups located at the sheet edges (Stankovich et al., 2006a), as shown in Figure 2.1. Although the introduction of functional groups weakens the mechanical properties of graphene, a mean elastic modulus of 32 GPa and tensile strength of 130 MPa of GO are still much superior to cement-based materials (Zhu et al., 2010, Dikin et al., 2007). These oxygen-containing functional groups render GO sheets hydrophilic and highly dispersible in water (Qiu et al., 2010b, Stankovich et al., 2006b), facilitating their dispersion in the cementitious matrix. Also, the 2D GO nanosheet offers a larger surface area for C–S–H nucleation than the much-researched CNTs, and those functional groups supply reactive sites that allow the development of strong bonds with C-S-H during nucleation (Lv et al., 2013).

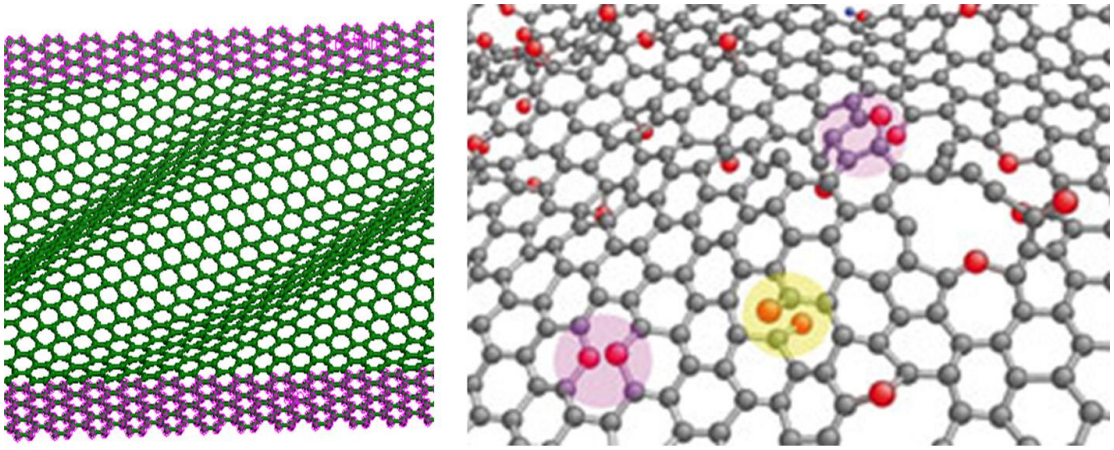

(a) (b)

Figure 2.1 (a) Wrinkled graphene (Duan et al., 2011) and (b) graphene oxide (Bagri et al., 2010)

Experimental investigations of GO-reinforced cement under static load have found significant improvement in mechanical properties. Introducing small quantities of GO, as little as 0.05 wt%, increased compressive strength by 15–33% and flexural strength by 41–59% (Pan et al., 2013). Typical curves are shown in Figure 2.2. The stress-strain curve indicates that the addition of GO improved the ductility and reduced the likelihood of sudden failure of cement, with GO/cement samples displaying a broader stress-strain curve within the post-peak zone. The increased strain capacity could be explained by delayed microcrack initiation.

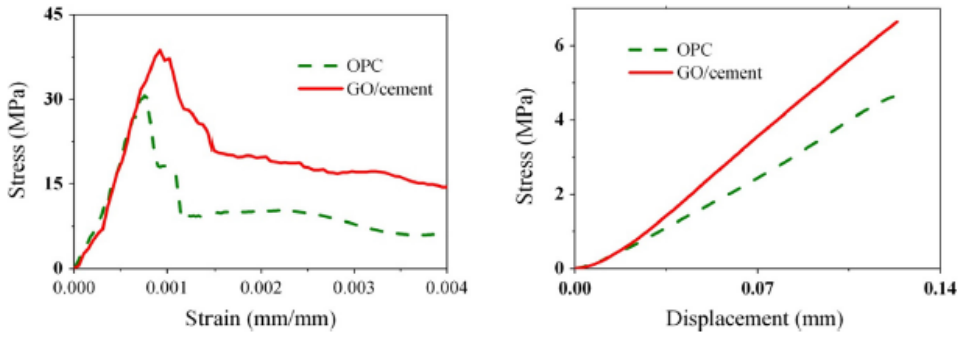

Figure 2.2 Effect of 0.05 wt.% GO: (a) Stress-strain curves under compression; (b) Load-displacement curves under flexure (Pan et al., 2013)

Laboratory tests also showed that the addition of 0.05 wt% GO improved pore structure and decreased total porosity from 32.6% to 28.2%, providing higher compressive strength and a more durable product (Pan et al., 2013). Kai (Gong et al., 2014) reported that the introduction of 0.03 wt% GO could increase the compressive strength and tensile strength of cement composites by more than 40%.

The existing research on GO-reinforced cement-based composites has mainly focused on the mechanical properties under static load, but the strain rate effect has not been studied.

2.3. Strain Rate Effect

2.3.1. Strain Rate Effect of Cement-Based Materials

Understanding the dynamic material properties of cement-based materials under high strain rates is essential for the design and modelling of cement-based material structures subjected to impact and blast loads. It is generally accepted that the dynamic strength of cement-based materials will increase when they are subjected to high strain rate (Ross et al., 1989, Malvar and Ross, 1998, Bischoff and Perry, 1991, Malvar and Crawford, 1998, Li and Meng, 2003, Zhang et al., 2009, Li et al., 2009). The dynamic increase factor (DIF), defined as the ratio of dynamic strength to static strength, is commonly used to represent the strength enhancement of the strain rate effect (Cotsovos and Pavlović, 2008). Attempts have been made by Bischoff and Perry (1991) and more recently by Cotsovos and Pavlović (2008) to assemble multiple sources of experimental data to identify the strain rate effect on concrete. Figure 2.3 and Figure 2.4 show the strain rate effect on concrete strength and the corresponding curve fittings, respectively. It has been reported that the DIF could potentially be higher than 6 in tension and higher than 2 in compression (Malvar and Crawford, 1998).

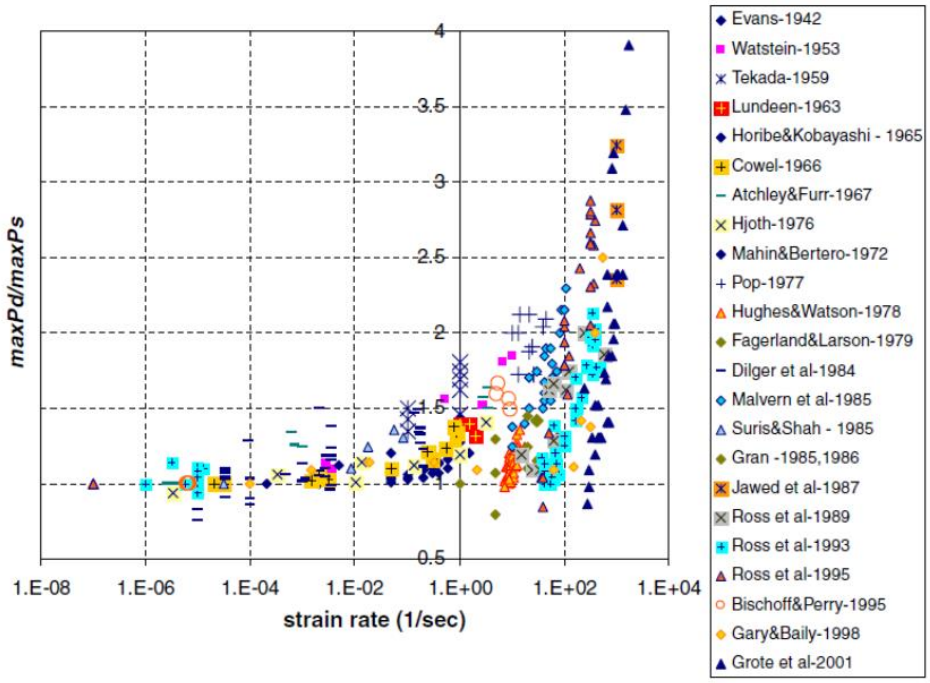

Figure 2.3 Variation of load-carrying capacity with strain rate for concrete in uniaxial compression (Cotsovos and Pavlović, 2008)

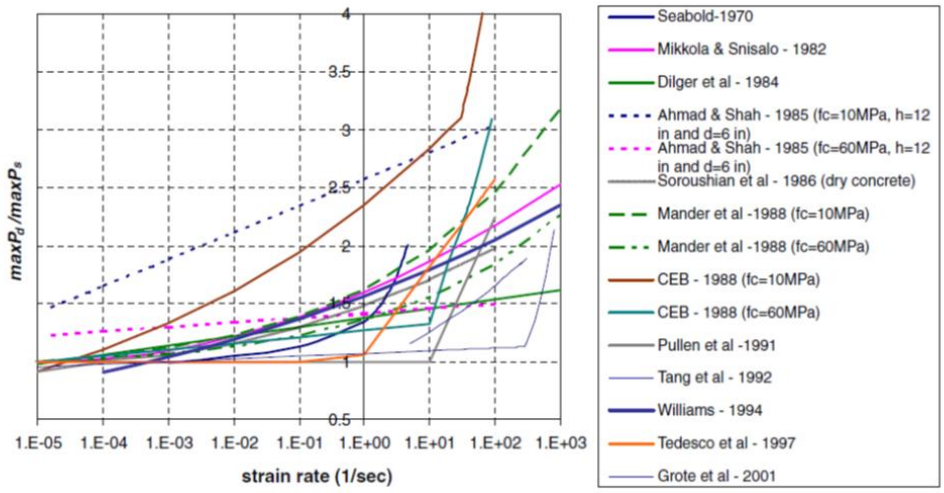

Figure 2.4 Best-fit curves of results obtained from uniaxial compression test (Cotsovos and Pavlović, 2008)

Compared with other materials such as metals and their alloys, the dynamic behaviour of cement-based materials is more complex due to its brittle nature and hydrostatic-stress-dependent property. Different mechanisms have been put forth to

explain the strain rate sensitivity of cement-based materials, including the effect of pore water, the effect of microcrack inertia, lateral confinement due to radial inertial effects and boundary (frictional) effects. The former two mechanisms can be regarded as intrinsic properties of cement-based materials, while the latter two can be classified as structural effects.

At strain rates below approximately 1.0 s^{-1}, the presence of free water dominates the strain rate effect, which is similar to the Stefan effect (Rossi and Toutlemonde, 1996). The Stefan effect is a phenomenon that occurs when a viscous liquid is sandwiched between two plates that are separated rapidly, leading to a reaction force acting on the plates (Rossi, 1991). Under a high strain rate, free water cannot be released from pores in a relatively short time and bears part of the strain rate loading. However, at a strain rate higher than 1.0 s^{-1}, the effect of pore water on dynamic strength is a second order factor in the overall increase of strength with strain rate (Brara and Klepaczko, 2006).

Nemat-Nasser and Deng (1994) suggested that the increase in compressive capacity with increasing strain rate could be a consequence of time-dependent microcrack growth. Under high strain rate loadings, the creation and propagation of microcracks are delayed due to the inertia effect (Tedesco and Ross, 1993). Therefore, the trapped energy cannot be released promptly through the crack formation, which may lead to the creation of tiny microcracks in a relatively strong area. This early stage microcrack diffusion will increase the strength of cement-based materials under high strain rate. On the other hand, it is known that crack propagation usually starts at the ITZ and then grows through the matrix (Giaccio and Zerbino, 1998). However, under a high strain rate, due to the rapid deformation of cement-based materials, the crack has not enough time to find the weaker section to develop, which causes the aggregates to

cleave (Brara and Klepaczko, 2006). Because of the higher strength of the aggregate than the matrix, the material strength of cement-based materials increases under a high strain rate.

Li and Meng (2003) suggested that, when the strain rate exceeds 10^2 s^{-1}, significant lateral confinement occurs and controls the dynamic compressive strength enhancement of cement-based materials. The lateral confinement results from both contact surface friction and lateral inertia during the rapid compression. Although the surface friction can be minimised by greasing the ends of the specimen, the lateral inertia can still strongly affect the strength of cement-based materials under high strain rate loadings. The reason why lateral inertia is so influential for cement-based materials is that the stress response of cement-based materials is hydrostatic stress dependent, which means that the radial pressure caused by the lateral inertia confinement affects the axial loading. In contrast is the case of the metallic specimen in which, because the lateral inertia induced lateral confinement does not influence the flow stress due to the important fact that the metal plasticity is hydrostatic stress independent, the influence of lateral inertia confinement is normally ignored (Li and Meng, 2003).

The above-mentioned mechanisms for strain rate sensitivity apply to plain cement-based materials without reinforcement. For nanoscale reinforcement-cement-based composites, the strain rate effect is still unknown.

2.3.2. High Strain Rate Test and Split Hopkinson Pressure Bar (SHPB)

At present, experimental methods to study material behaviour under high strain rate loadings are often costly and labour intensive (Field et al., 2004). Figure 2.5 shows the different types of experimental techniques corresponding to different ranges of strain rate. Due to its simplicity and robustness, the SHPB is the most widely used

experimental technique to study dynamic material properties with strain rates ranging from 10^2 to 10^4 s^{-1} (Field et al., 2004).

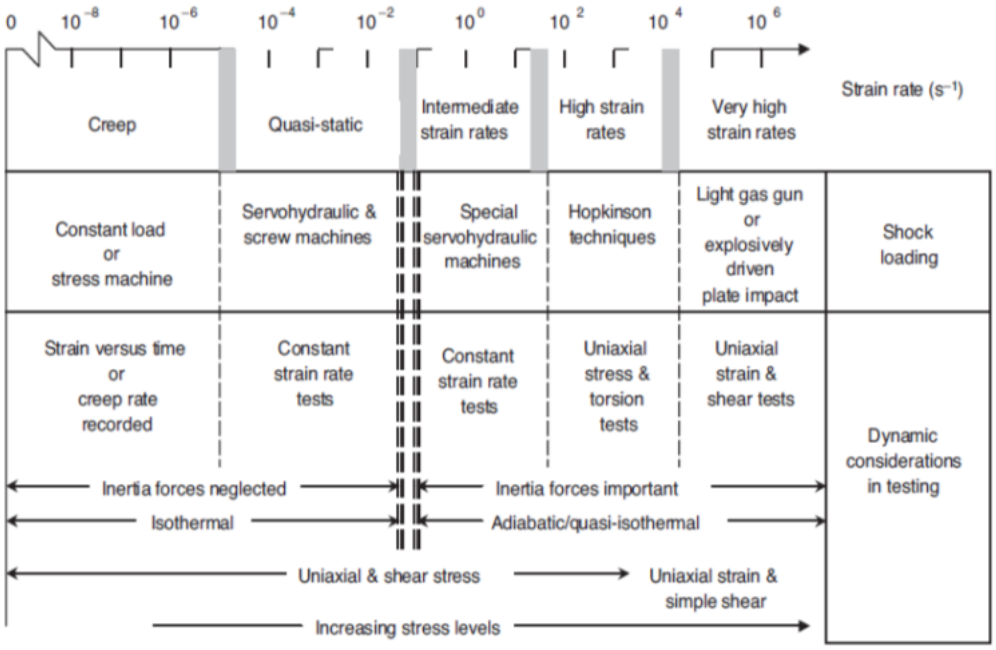

Figure 2.5 Strain rate regime and corresponding experimental techniques (Nemat-Nasser, 2000).

The prototype of the SHPB technique is a stress wave test in iron wires invented by John Hopkinson in 1872 (Hopkinson, 1872). It was modified by Kolsky in 1949 (Kolsky, 1949) to measure the compression behaviour of different materials under dynamic loadings. A typical experimental setup of the SHPB test is shown as Figure 2.6. The specimen is sandwiched between two long slender bars. When the strike bar, propelled by the gas gun, impacts the incident bar, a stress wave is generated and travels through the bar towards the specimen. When the wave reaches the specimen, part of the stress wave is reflected back to the incident bar and the remainder is transmitted through the specimen into the transmitter bar. The remaining energy in the transmitter bar is absorbed by the momentum bar. Two strain gauges are mounted on the bars and connected with an oscilloscope to collect the data. By collecting the data read from the

strain gauges, the stress, strain and strain rate can be calculated. Varying the velocity of the strike bar can achieve different strain rates in the specimen. In this study, the SHPB was used as the experimental method for high strain rate testing.

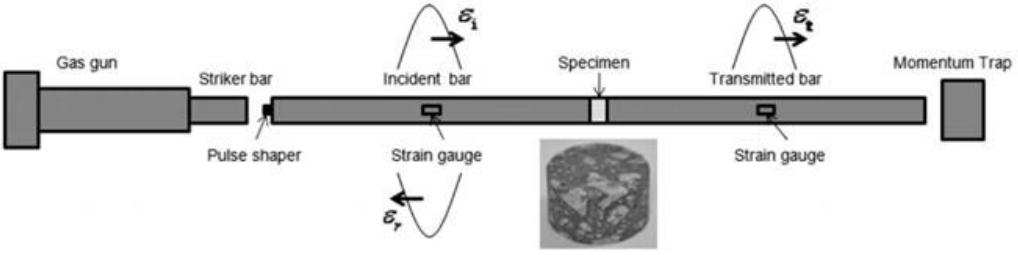

Figure 2.6 Typical SHPB test setup. Reproduced from Wu et al. (2010)

2.4. Numerical Investigations

2.4.1. MD Simulations of Nanoscale Reinforcements

To understand the reinforcing mechanisms of nanoscale reinforcements, the key is to find out the interaction properties between the nanoscale reinforcement and the matrix, which determines the efficiency of stress transfer from the matrix to the reinforcement (Coleman et al., 2006). Because of the technical difficulties involved in the manipulation of nanoscale reinforcements of extremely small size, direct experimental measurements are severely hampered (Tsuda et al., 2011, Gou et al., 2004). On the other hand, continually increasing computing power has facilitated the investigation of atomistic interactions by MD simulation.

MD simulation has been used by many researchers to simulate the pull-out behaviour of nanoscale reinforcements from polymers. Gou et al. (2004) conducted MD simulations on single wall carbon nanotube (SWCNT) pull-out from cured epoxy resin and calculated the interfacial shear strength as 75MPa. Liao and Li (2001) reported a

numerical study of the double-wall CNT-polystyrene composite system by MD simulation and characterized the interfacial shear strength as 160 MPa.

In contrast, numerical simulation of nanoscale reinforcements-cement composites is rarely seen in the literature. Calcium silicate hydrate (C-S-H) is the main hydration product of cement. It is widely accepted that C-S-H has a layered structure akin mostly to that of tobermorite and jennite minerals (Shahsavari et al., 2009). The crystal chemical formula of jennite is given as $Ca_9Si_6O_{18}(OH)_6 \cdot 8H_2O$ (Bonaccorsi et al., 2004). Compared with tobermorite, the Ca/Si ratio of jennite (1.5) is closer to that of C-S-H gel (1.7) as proposed by Allen et al. (2007). Therefore, jennite mineral has been adopted by many researchers as the crystal model to simulate the C-S-H structure (Hou and Li, 2013, Moon et al., 2015, Al-Ostaz et al., 2010). In the MD simulations in Chapter 4, the jennite crystal structure was also used as the C-S-H model.

2.4.2. Crack Bridging Model for Fibre-Reinforced Cementitious Composites

In fibre-reinforced cement-based composites, crack bridging is the main reinforcing mechanism (Li et al., 1993, Bentur and Mindess, 2006). When a crack opens, the fibre crossing the crack plane is subjected to the pull-out force. The load-carrying capacity of cement-based composites is affected by the post-cracking stress-crack separation relationship. To quantify the reinforcing effect of fibres, Li proposed a micromechanics based crack-bridging stress-crack opening model (C. Li, 1992), which is also one of the most widely used micromechanical models for fibre-reinforced cement-based composites. His model was the first to establish the relationship between the pull-out force and the pull-out displacement for a single fibre. By assuming that the fibres have a 3D random distribution and orientation in the matrix, the position and orientation of a single fibre can be determined uniquely by three parameters, fibre length L_f, distance

between the fibre centroid and the matrix crack plane *z*, and the orientation angle φ, as shown in Figure 2.7. Then the crack-bridging stress σ_B can be predicted by integrating the contributions of all the fibres crossing the crack plane.

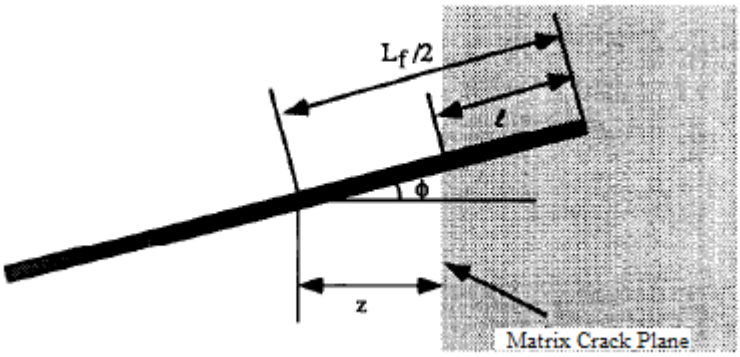

Figure 2.7 A fibre crossing a matrix crack plane (Li et al., 1991)

Although Li's model was originally proposed for microfibre-reinforced cement-based composites, it can be modified for nanoscale fibres. Chen et al. (2014) extended Li's model to CNT reinforced composites. In that extended model, the length distribution and dispersion of CNT fibres were also considered. The effectiveness of the extended model has been validated by good agreement between the model predictions and experimental results (Zou et al., 2015).

However, the above-mentioned crack bridging models are both for 1D fibre reinforced composites, and there are no models available for composites reinforced by 2D sheets.

2.4.3. Finite Element Simulations Using Microplane Model

Most of the existing constitutive models for cement-based materials can be classified into the classical approach, in which the material model is formulated directly in terms of stress and strain tensors and their invariants (Bazant et al., 2000b). However, these macroscopic tensorial models cannot capture the interactions of cement-based materials

at microscale. In GO-reinforced cement-based composites, the interactions between the reinforcements and the matrix are at the scale of micro- or even nano-level. Therefore, micromechanical models that can develop macroscopic stress-strain relationships from the mechanics of the microstructure (Babu et al., 2005) are expected. A popular model in this category is the microplane model developed by Bazant and his colleagues since 1983. The microplane model formulates its constitutive law in terms of vectors rather than tensors (Bazant et al., 2000b). The relation between the stress and strain components is defined on a plane of any orientation in the material microstructure, called the microplane (Bažant, 1984). The macroscopic strain and stress tensors are calculated as the summation of the vectors on the microplanes under the kinematic constraint. The basic relations of microplane model are briefly explained below. The basic hypothesis is that the normal and shear strain on each microplane are projections of $\boldsymbol{\varepsilon}$ (Figure 2.8)

$$\varepsilon_N = N_{ij}\varepsilon_{ij}, \varepsilon_L = L_{ij}\varepsilon_{ij}, \varepsilon_M = M_{ij}\varepsilon_{ij} \quad (2.1)$$

The subscript *N* refers to the normal direction, while *L* and *M* refer to the shear direction.

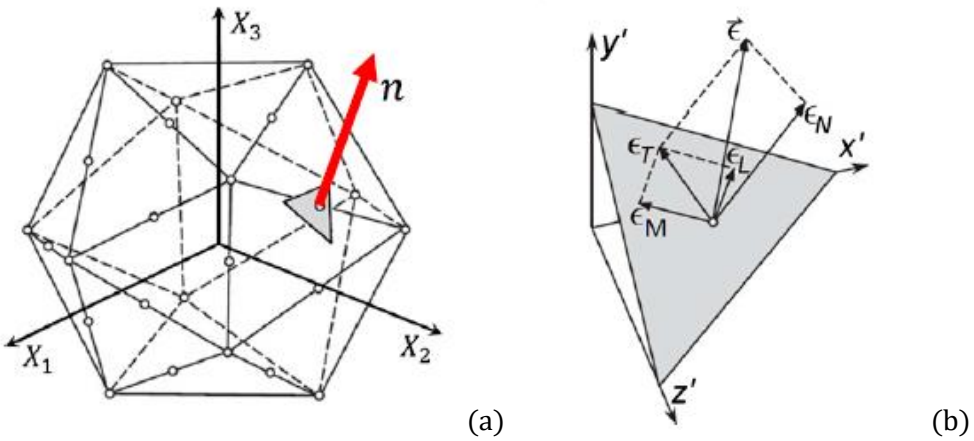

(a) (b)

Figure 2.8 (a) Microplane strain vector; (b) microplane strain components. Reproduced from (Caner and Bažant, 2012)

The static equivalence of stresses between the stress vectors on all the microplanes and the stress tensor can be enforced by the principle of virtual work (Bažant, 1984)

$$\frac{2\pi}{3}\sigma_{ij}\,\delta\varepsilon_{ij} = \int_{\Omega}\left(\sigma_N\,\delta\varepsilon_N + \sigma_L\,\delta\varepsilon_L + \sigma_M\,\delta\varepsilon_M\right)\mathrm{d}\Omega \tag{2.2}$$

where Ω = surface of a unit hemisphere centred at the material point; and $2\pi/3$ = its volume.

Another feature of the microplane model is the way it controls the strain-dependent yield limits. The stress-strain boundary is defined such that if the boundary is exceeded in a finite load or time step, the stress is reduced to the boundary, keeping the strain constant (Caner and Bažant, 2012). It should be pointed out that the tensile behaviour is determined by the normal boundary σ_N.

Since 1983, a series of microplane models labelled M0, M1, M2, …, M7 has been developed for concrete and the up-to-date version is M7 (Caner and Bažant, 2012, Bazant, 2013). A dozen advantages of the microplane model for characterizing the material behaviour were reviewed by Brocca and Bazant (2000) and Bazant et al. (2000b). One of the most important advantages is its capability of capturing the interactions among orientations of microdamage processes (e.g., orientations of tensile or splitting microcracks, and frictional microslips) (Bazant, 2010). This advantage is verified by the successful capture of the so-called vertex effect using the microplane model (Caner et al., 2002), which cannot be captured by classical tensorial models with one or a few loading surfaces (Caner and Bažant, 2012). Applications of microplane models in the field of concrete structures are relatively limited. M4 has been adopted in investigation of the size effect of concrete columns (Brocca and Bazant, 2001), the tube squash test of concrete (Brocca and Bažant, 2001) and mixed-mode fracture in concrete (Ožbolt and Reinhardt, 2002), to name a few.

2.5. Research Gaps

Based on the above literature overview, the following research gaps can be identified:

(1) No investigation has been reported of the mechanical properties of nanomaterial-reinforced cement-based composites under high strain rate. Whether the inclusion of GO will affect the strain rate sensitivity of cement-based composites is still unknown.

(2) Understanding of the interactions between GO and cement matrix is still very limited and no quantitative description of their interactions is available.

(3) No crack bridging model has been reported for composites reinforced by 2D ATM such as GO.

(4) No finite element simulation has been reported for GO-reinforced cement-based composites and no constitutive model has been reported to be suitable for the simulation of GO-reinforced cement-based composites.

These research gaps are addressed in the following chapters.

CHAPTER 3. EXPERIMENTAL RESULTS OF GO-REINFORCED CEMENT MOTAR UNDER STATIC AND HIGH STRAIN RATE LOADINGS

3.1. Introduction

In this chapter, the experimental results of GO-reinforced cement mortar are reported. Both plain cement mortar (control) samples and GO-reinforced cement mortar (GO-mortar) samples were fabricated and tested. Tensile splitting and compression tests were conducted under both static loadings and high strain rate loadings. The high strain rate testing was performed using a Split Hopkinson Pressure Bar (SHPB) apparatus. The effect of high strain rate on the tensile splitting and compressive strength of GO-mortar were compared with results from the plain cement mortar. Fragments of the samples after SHPB testing were collected to observe the failure mode. From analysis of the experimental results and the failure modes, the reinforcing effect of GO under static and high strain rate loadings were explored and discussed.

3.2. Experimental Program

3.2.1. Materials

The GO solution was supplied by Graphenea®. The concentration of GO nanosheets in the solution was 4mg/ml. Based on the scanning electron microscope (SEM) image of the GO nanosheets, as shown in Figure 3.1, the mean size of GO was about 1 μm.

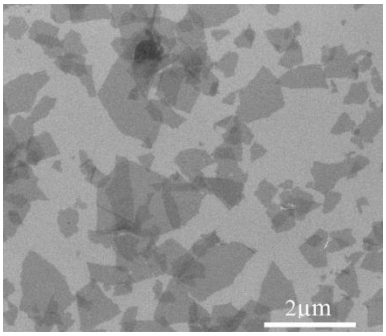

Figure 3.1 SEM image of GO nanosheets (Li et al., 2016a)

As defined by ASTM C150 (C150, 1999), general purpose ordinary Portland cement (OPC), conforming to the requirements of Type I – Normal cement, was used for all the samples. Table 3-1 shows the chemical composition of the cement powder as analysed by X-ray fluorescence.

Table 3-1 Chemical compositions of cement powder

Al_2O_3	SiO_2	CaO	Fe_2O_3	K_2O	MgO	Na_2O	SO_3	LOI
4.7	19.9	63.9	3.4	0.5	1.3	0.2	2.6	3.0

The sand adopted in this study was high purity silica sand (commercially available product of Sibelco, Australia). As can be seen from the particle size distribution of the sand, shown in Figure 3.2, the mean size of the sand was about 0.45mm.

A polycarboxylic based superplasticiser (SP) (commercially available as ADVA 210, a product of WR Grace) was used to modify the workability of the mortar.

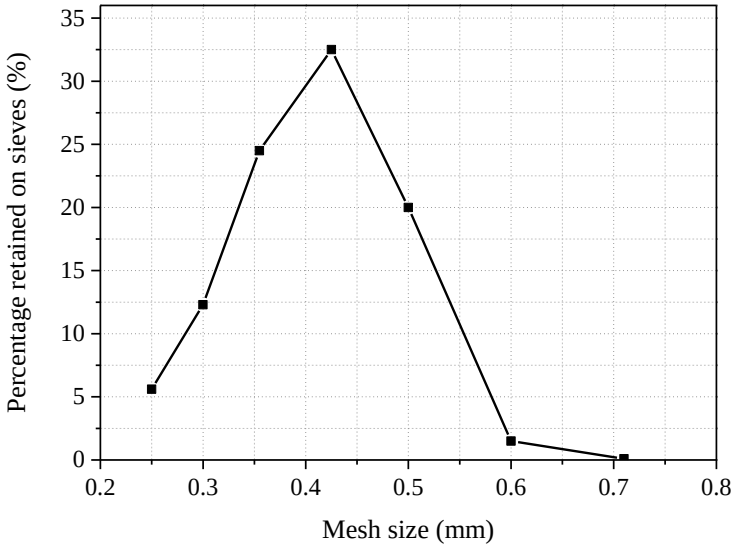

Figure 3.2 Particle size distribution of sand (Li et al., 2016b)

3.2.2. Mix Design and Mixing Procedure

Table 3-2 shows the mix design of the mortar samples. The mass ratios of sand to cement and water to cement were the same for all the samples: 2 and 0.4, respectively. The control samples without GO nanosheets were denoted M. Two series of GO-mortar samples with GO concentration of 0.02 wt% and 0.04 wt% were designed and denoted MG2 and MG4. To improve the interfacial zone between silica sand and cement and disperse GO better, a new mixing procedure was adopted. The sand was first mixed with water and GO solution, and then mixed with cement and SP. The detailed mixing procedure can be found in (Li et al., 2016b). Flow table tests conforming to ASTM C1437-15 (C1437-15, 2015) were conducted to measure the workability of the fresh mixtures. The SP was first added to control samples to improve its workability. Then the SP dosages for MG2 and MG4 were adjusted to achieve similar workability to that of the control samples.

Table 3-2 Mix design of the mortar samples

	M	MG2	MG4
Water/cement (by weight)	0.4	0.4	0.4
Sand/cement (by weight)	2	2	2
GO/cement (wt. %)	0	0.02	0.04
SP/cement (wt. %)	0.55	0.70	0.85

After mixing, the fresh mixtures were cast into moulds and vibrated on a vibration table to achieve good compaction. The moulds were then sealed with polyethylene sheets to retain moisture. The samples were demoulded after 24h and then cured in a saturated lime water bath at 20 °C until testing. For both static and high strain rate experiments, the samples were tested at the age of 28 days.

3.2.3. Tests Quasi-static Splitting Tensile and Compression Tests

Cylindrical mortar specimens (Ø23.5 × 47mm) were used for the static tensile splitting and compression tests. For the tensile splitting tests, the loading rate was set to 2kN/min, conforming to ASTM C496 (C496/C496M-11, 2004). For the compression tests, following ASTM C109 (C109/C109M-16, 2016) , the loading rate was set to 0.2mm/min, corresponding to approximately 0.3MPa/s. A Shimadzu testing machine with the capacity of 300 kN was used to conduct both the static tensile splitting and compression tests.

3.2.4. Setup and Data Processing of SHPB

The SHPB technique has been widely adopted over recent decades in research into cement-based materials under high strain rate loadings, with a strain rate ranges from 10 to 10^4 s^{-1} (Tedesco et al., 1994). The experimental set-up of SHPB comprises two

long slender aluminium bars with a short specimen sandwiched between them, as shown in Figure 3.3. When the strike bar impacts the incident bar, a stress wave is generated and travels through the bar towards the specimen. When the wave reaches the specimen, part of the stress wave is reflected back to the incident bar and the remainder is transmitted through the specimen into the transmitter bar. The remaining energy in the transmitter bar is absorbed by a damper.

As shown in Figure 3.3, cylindrical mortar specimens (Ø13 × 13 mm) were tested using a 14.5 mm (diameter of strike, incident and transmitter bar) SHPB testing system. The specimen arrangement in the tensile splitting tests is also indicated in Figure 3.3.

Two sets of data were collected by an oscilloscope connected to strain gauges (SG1 and SG2) on the incident and transmitter bar respectively. The strain gauges used in this study were more sensitive semiconductor strain gauges rather the conventional foil strain gauges. The SB2-120-P-2 semiconductor strain gauges (commercially available product of Bestech, Australia) have a gauge factor of about 110, whereas the gauge factor of conventional foil strain gauges is about 2.1.

On the basis of the assumption of 1D wave propagation, the stress of the tensile splitting and compression SHPB tests can be obtained by:

$$\sigma_s(t) = \left(\frac{A_B E_B}{A_{s0}}\right) * \varepsilon_T(t) \tag{3.1}$$

The strain rate of the SHPB compression test can be calculated by:

$$\dot{\varepsilon}_c(t) = \left(\frac{2c_{0B}}{H_{s0}}\right) * \varepsilon_R(t) \tag{3.2}$$

For the SHPB tensile splitting test, the equation of strain rate is given by:

$$\dot{\varepsilon}_t(t) = \frac{f_t / \tau}{E_{s0}} \tag{3}$$

where A_B and A_{S0} are the cross section area of the bar and the specimen, respectively; E_B is the Young's modulus of the incident and transmitter bar; $\varepsilon_T(t)$ and $\varepsilon_R(t)$ are the transmitted and reflected wave, respectively; c_{0B} is the elastic wave speed of the incident and transmitter bar; Hs_0 is the length of the specimen; E_{S0} is the static Young's modulus of the specimen; f_t is the maximum tensile stress of the specimen; τ is the time lag between the start and the peak of the transmitted wave.

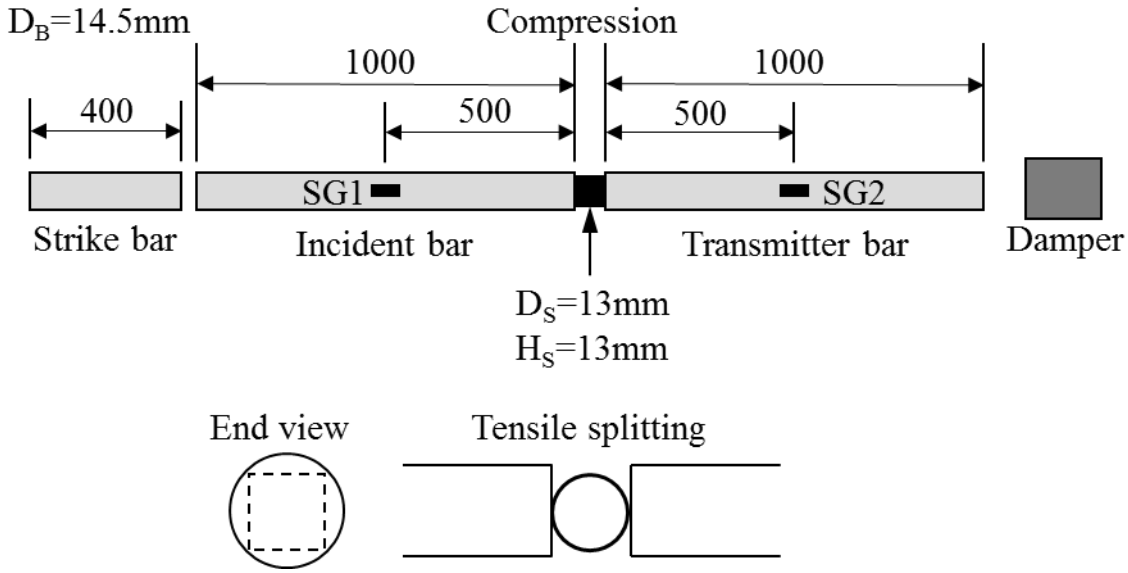

Figure 3.3 SHPB set-up

3.3. Results and Discussion

3.3.1. GO Identification

Figure 3.4 shows SEM images of the sand surface after mixing with GO solution. It can be seen from Figure 3.4-a that the region around point 1 was bald, without GO nanosheets, while the remaining part was covered by GO. The area within the yellow box is magnified in Figure 3.4-b. The unique wrinkled shape of the GO is quite obvious.

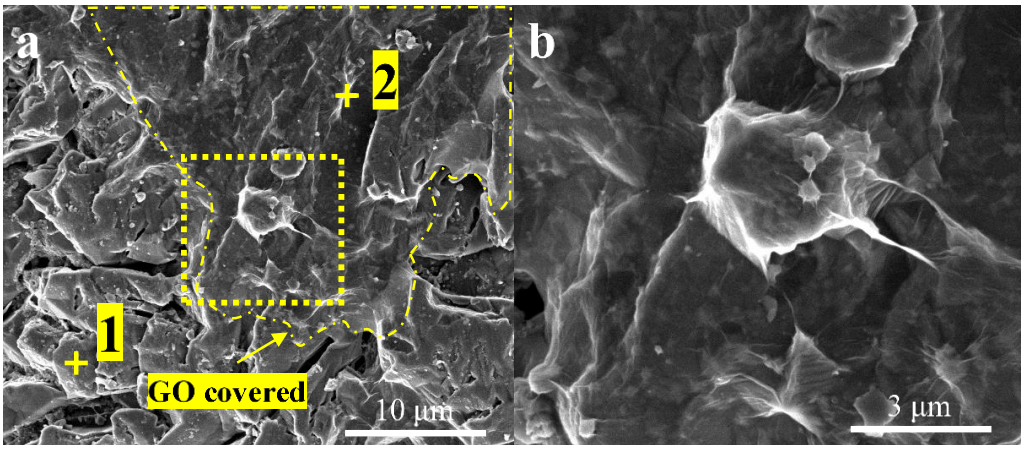

Figure 3.4 SEM images of sand surface with GO

The existence of GO was further identified by energy-dispersive X-ray spectroscopy (EDS) analysis, as shown in Figure 3.5. It can be seen that the signals of carbon and oxygen at point 2 (in Figure 3.4-a) are much stronger than those at point 1, indicating that the region around point 2 was covered by GO, unlike that around point1.

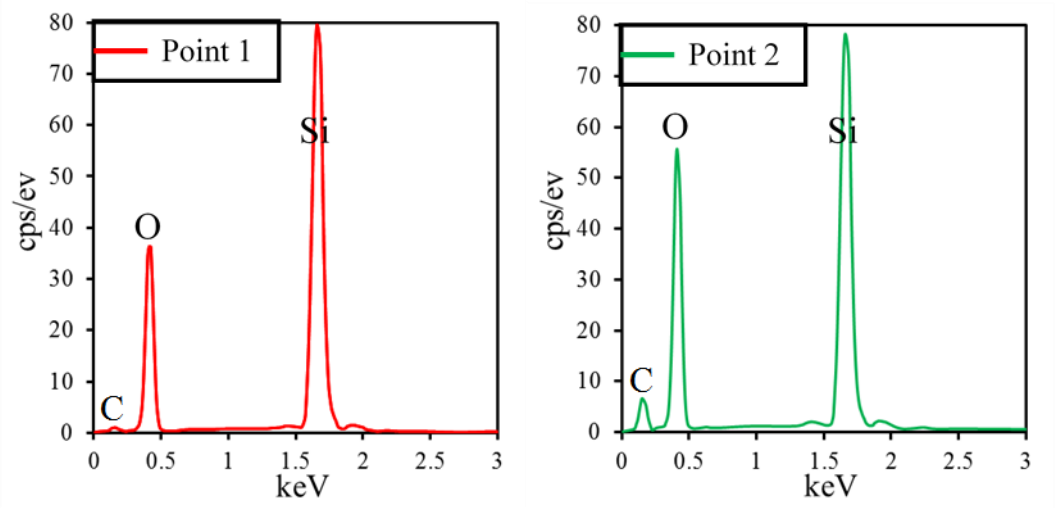

Figure 3.5 EDS spectra of point 1 (with GO) and point 2 (without GO)

3.3.2. Static Tests

Figure 3.6 shows the static tensile splitting strength of the control samples and GO-mortar samples. Incorporation of 0.02% and 0.04% GO increased the tensile splitting strength by 8.9% and 9.9% respectively.

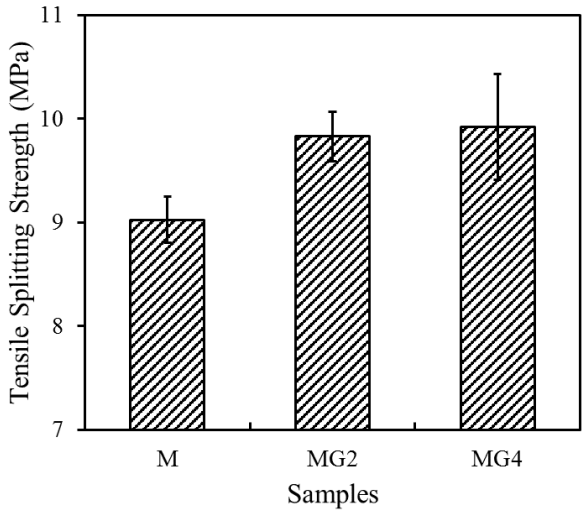

Figure 3.6 Static tensile splitting strength

Figure 3.7 shows the static compressive strength of the control samples and GO-mortar samples. Incorporation of 0.02% and 0.04% GO increased the compressive strength by 10.8% and 13.4% respectively.

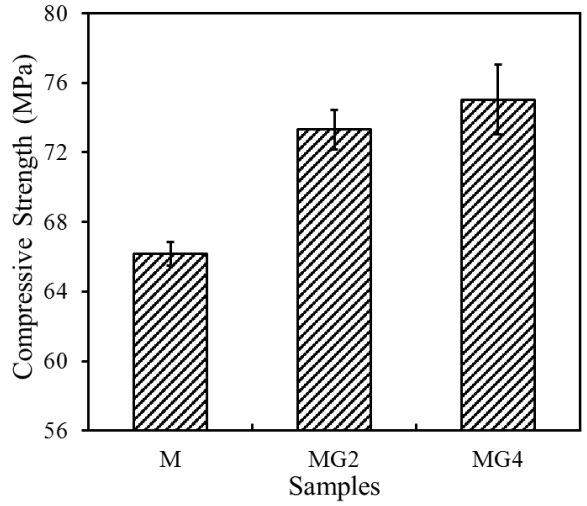

Figure 3.7 Static compressive strength

According to the results, there was little difference between the strength increase of 0.02 wt% GO addition and 0.04 wt% GO addition in both static tensile splitting and compression tests. It appears that the incorporation of GO had a slightly greater impact on compression strength than on tensile splitting strength. Different mechanisms have been raised to explain the reinforcing effect of GO on mortar composites (Li et al., 2016b). First, the incorporation of GO can improve the mechanical properties of cement paste bulk (Pan et al., 2015, Gong et al., 2014). In addition, because the presence of GO in the surfaces of silica sand, acting as nucleation sites, can promote the hydration and production of calcium silicate hydrate (C-S-H), the ITZ of GO mortar samples is denser and stronger than that of control samples (Li et al.).

3.3.3. Tensile Splitting and Compressive Strength under High Strain Rate Loadings

Figure 3.8 shows the tensile splitting strength of control samples and GO-mortar samples under high strain rates. As can be seen, the strength of both the control samples and the GO-mortar samples was rate-dependent and increased along with the increase of the strain rate. This phenomenon is consistent with the findings for plain cement-based materials and microfibre-reinforced cement-based composites. Various researchers have discussed the mechanisms causing the strain rate effect of cement-based materials (Tedesco et al., 1993, Nemat-Nasser and Deng, 1994, Li and Meng, 2003). At low strain rates, a crack will find the weakest path to propagate. Under high strain rates, however, there is no time for a crack to find weak a section to propagate, and the cracks are thus more direct, passing through stronger areas, for example causing the aggregates to cleave (Brara and Klepaczko, 2006, Feng et al., 2014). Therefore, more energy is consumed in the crack propagation and the material strength is higher under a high strain rate.

To evaluate and compare the strain rate effect of control samples and GO-mortar samples, the DIF of the specimens under tensile splitting is illustrated in Figure 3.9. It can be seen that the DIF of the GO-mortar samples and the control samples were similar under different strain rates, indicating the strain rate effect of the GO-mortar samples was similar to that of the control samples. Thus, in the tensile splitting tests, the reinforcing effect of GO on mortar composites was the same for static and high strain rate loadings and the inclusion of GO had no extra reinforcing effect under high strain rate loadings.

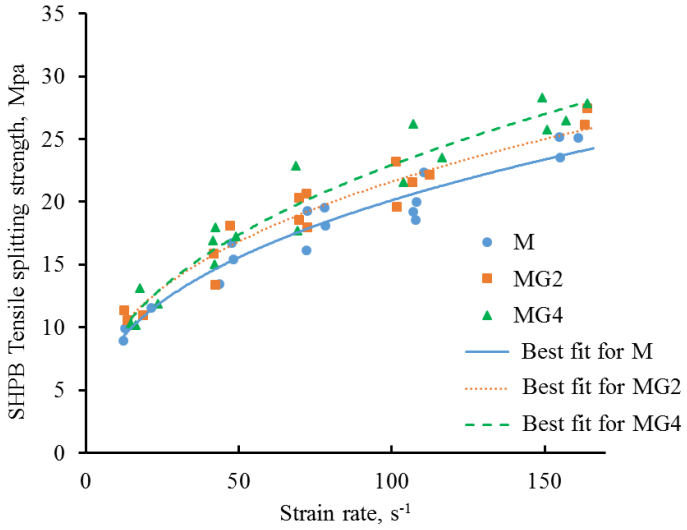

Figure 3.8 Tensile splitting strength under high strain rate

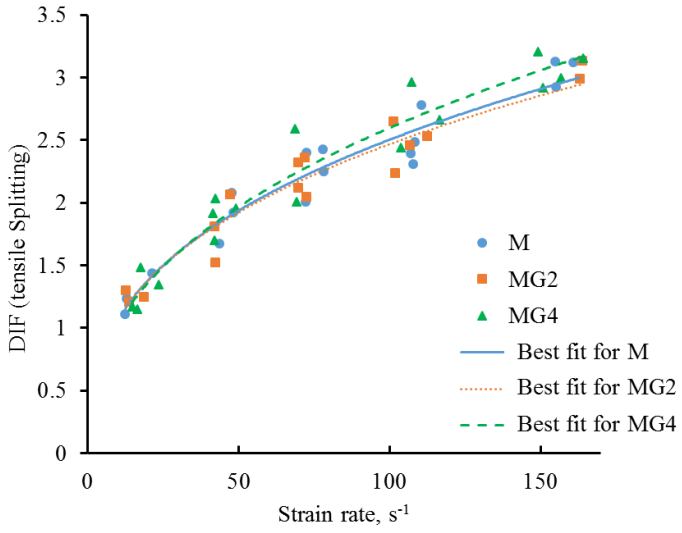

Figure 3.9 DIF of specimens under high strain rate tensile splitting tests

Figure 3.10 shows the compressive strength of control samples and GO-mortar samples under high strain rate loadings. As in the tensile splitting SHPB tests, an increase in the strain rate led to an increase in the dynamic compressive strength of both the control and the GO-mortar samples. However, compared to the control samples, the strength increase of the GO-mortar samples was more significant at higher strain rates. This phenomenon is further illustrated in Figure 3.11. The DIFs of the GO-mortar and control samples were similar under lower strain rates, but at higher strain rates the DIF of the GO-mortar samples was significantly higher than that of the control samples. This result means that in compression testing, besides the reinforcing effect of GO under static loadings, the inclusion of GO had an additional reinforcing effect under high strain rate loadings and this effect became more significant under higher strain rates.

These results are different from the findings of strain rate effect in microfibre-reinforced cement-based composites. It has been reported that the DIF for compressive strength of plain concrete is higher than that of corresponding fibre-reinforced concrete at given high strain rate (Wang et al., 2012b). [30]. Moreover, a higher fibre volume

content, regardless the fibre type, leads to a lower DIF value for a certain strain rate (Tran and Kim, 2014). Different mechanisms have been suggested to explain these phenomena. In fibre-reinforced composites there is a group effect for the fibres, which means that when a group of fibres interact with each other during pull-out, the strain rate sensitivity is less than that of a single fibre pull-out (Naaman and Shah, 1976, Tran and Kim, 2014) Moreover, if the fibre volume content is high, the amount of matrix surrounding the fibre may not be sufficient to maintain interfacial bonding, which could result in a diluted or eliminated strain rate sensitivity (Tran and Kim, 2014). In GO-reinforced cement-based composites, however, these mechanisms might no longer be valid. Because of the low volume percentage and extremely small size of GO, the GO sheets can scarcely interact with other and there is also enough matrix to maintain the interfacial bonding with GO.

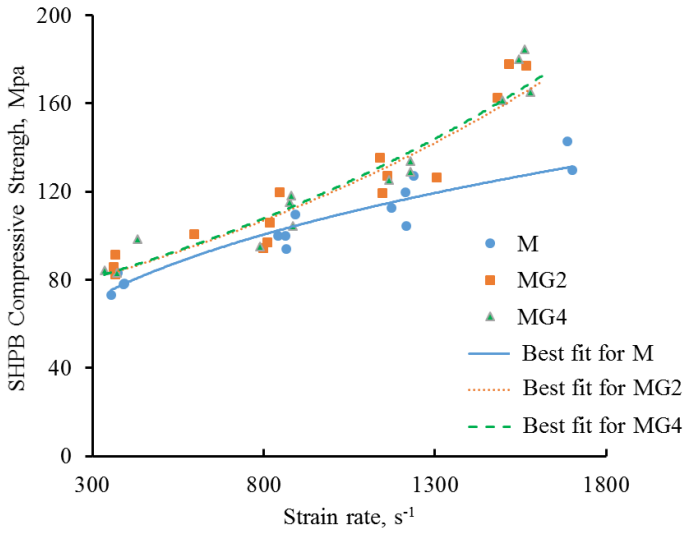

Figure 3.10 Compressive strength under high strain rate

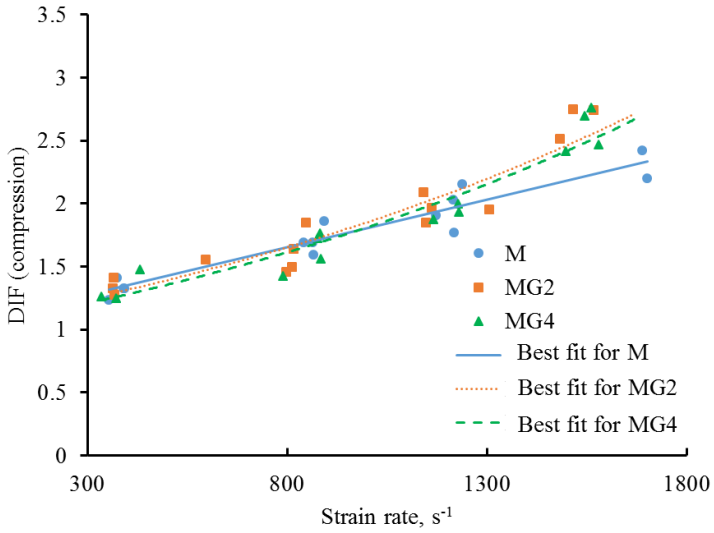

Figure 3.11 DIF of specimens under high strain rate compression tests

3.3.4. Analyses of Failure Modes and GO Reinforcing Effect under High Strain Rate

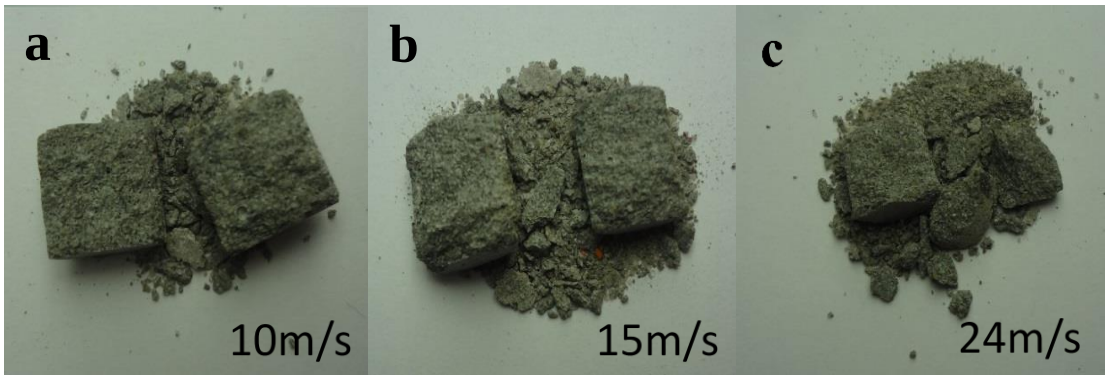

Figure 3.12 Fragments of specimens under high strain rate tensile splitting loading

To explain the different reinforcing effects of GO in high strain rate tensile splitting and compression testing, fragments of the samples after SHPB testing were accumulated and analysed. Figure 3.12 and Figure 3.13 show the fragments of specimens after SHPB tensile splitting and compression tests with different strike bar speeds of 10m/s, 15m/s and 24m/s.

Figure 3.13 Fragments of specimens under high strain rate compression loading

It must be mentioned that the difference between the distribution of fragments of the control samples and the GO-mortar samples was minimal, so the fragments shown in Figure 3.12 and Figure 3.13 are all from MG4 samples. As can be seen, in general, the higher the strain rate, the larger number and smaller size of the fragments. However, this fragmentation effect was much more significant in the compression test than in the tensile splitting test.

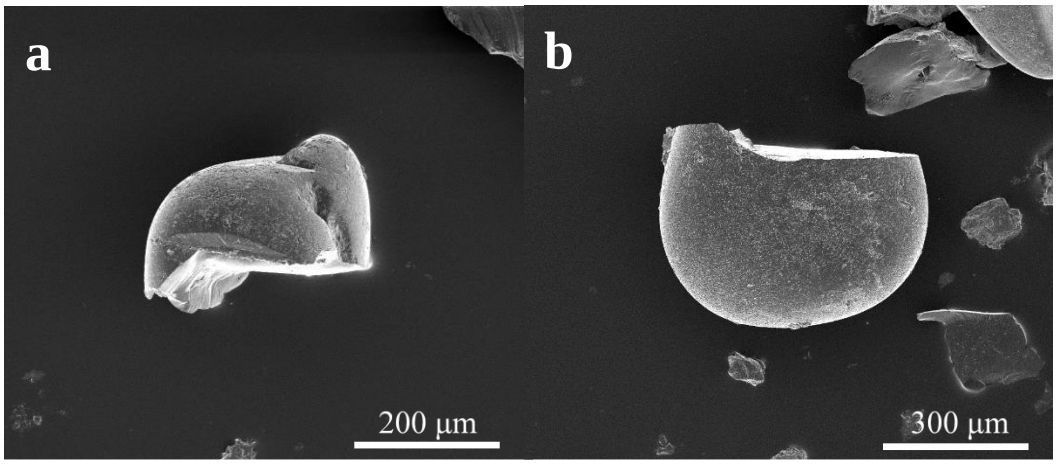

Figure 3.14 SEM images of sand fragments under high strain rate loadings

As mentioned already, under high strain rates a crack can propagate through a stronger area and sometimes cause cleavage of the aggregates. But it is still unknown whether the fine aggregates used in this study, with a mean size of only 0.45mm, can

be cleaved. Figure 3.14 shows SEM images of cleaved sand, which were captured after the compression SHPB tests of MG4 sample with the highest strain rate. Similar phenomena can be also observed for the M and MG2 samples. This finding indicates that cracks can penetrate through fine sand and manifests, on the other hand, the degree of fragmentation of the samples after SHPB testing.

A more detailed fragmentation analysis was conducted, as shown in Figure 3.15. Fragments of the control samples and GO-mortar samples after SHPB testing with different strike bar speeds were collected and separated by a 3.5mm sieve. Then the weights of the small and large fragments were measured and compared. The mass ratio was defined as the ratio of the mass of small fragments over the mass of large fragments. It was found that from the tensile splitting SHPB tests, the mass ratio kept increasing but was less than 1 even at the highest strike bar speed. For the compression tests, however, the mass ratio increased dramatically and at the highest speed, the mass of small fragments was more than a tenth of the mass of large fragments.

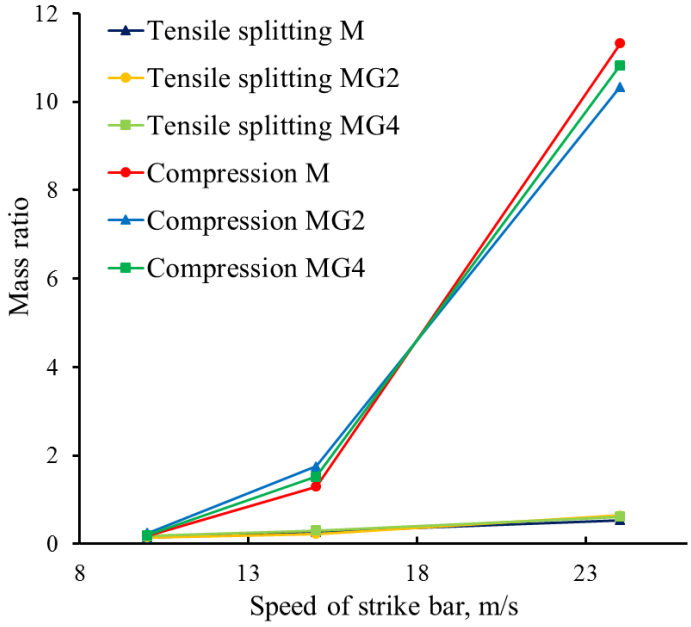

Figure 3.15 Mass comparison after separation by a 3.5mm sieve

The difference between SHPB tensile splitting and compression tests in terms of fragment distribution and mass ratio can be attributed to the different failure modes of tensile and compression tests under high strain rates. In tensile splitting tests, the major crack was always located in the centre of specimens, regardless of the strain rate. In compression tests, on the other hand, the cracks were diffused all over the entire sample and, under higher strain rates there was a significant increase in the number of cracks, creating many more fracture surfaces. The higher number of cracks and the larger area of fracture surfaces meant a higher possibility of a crack passing through the GO nanosheets, which made the reinforcing effect of GO more significant.

3.4. Conclusions

In this study, the tensile splitting and compressive strength of GO reinforced mortar composites were tested under both static and high strain loadings. Two concentrations of GO, 0.02% and 0.04% by weight of cement, produced similar results for all the experiments. With the incorporation of GO, both the static tensile splitting and the compressive strength were improved and the improvement in compressive strength was slightly higher than that in tensile splitting strength. The SHPB tests showed that the reinforcing effect of GO under a high strain rate was directly related to the number of cracks. In tensile splitting tests, because the major crack is always located in the centre of the specimen regardless of the strain rate, the reinforcing effect of GO on the mortar is the same for different strain rates. In compression tests, however, because the cracks are diffused and there are more cracks under higher strain rates, the reinforcing effect of GO is also more significant under a higher strain rate.

CHAPTER 4. MD SUMULATION AND A NEW CRACK BRIDGING MODEL FOR ATOMICALLY THIN MATERIALS REINFORCED COMPOSITES

4.1 Introduction

In this chapter, MD simulations were conducted to investigate the pull-out behaviours of atomically thin materials such as GO from different matrices such as C-S-H. This research is not limited to GO and C-S-H matrix but extended to 2D atomically thin materials and different types of matrices. Conversely, the findings and conclusions from this study are also applicable to GO-reinforced cement-based materials.

Atomically thin materials (ATMs), such as graphene and its derivatives, are among the best candidates for enhancement of biomaterials [1-3], polymer [4-10], metal [11-14] and ceramic/cementitious materials [15-18] because of their superior mechanical properties. It is reported that the elastic modulus of chitosan can increase over ~200% with the addition of 0.1-0.3 wt% graphene [1]; inclusion of 0.7 wt% graphene oxide (GO) can increase the tensile strength and Young's modulus of polyvinyl alcohol (PVA) by 76% and 62% [10]; the tensile strength of aluminium composite reinforced by 0.3 wt% graphene achieve a 62% enhancement over the unreinforced aluminium matrix [11]; with the addition of 0.8 vol% graphene, the fracture toughness of alumina ceramic can be increased by 40% [15]; the compressive strength and flexural strength of cement can increase by 15-33% and 41-59% with the introduction of 0.05 wt% GO [18]. Thus ATMs may be the key to producing stronger next-generation materials.

The pull-out of nanometer scale reinforcements during fracture is one of the major mechanisms for enhancing mechanical properties [19, 20]. During pull-out, the interaction between the embedded reinforcement and the matrix, e.g. friction and

chemical bonding, consumes energy, so that more energy is needed to open cracks and any failure of the material is delayed [21, 22]. A major advantage of using nanosized super-strong reinforcements, such as graphene, is that they can bridge the finest cracks in the material, preventing crack propagation and further damage [17, 23-26].

Although many studies have explored the improvement of mechanical properties using ATMs [1-18], investigation of the governing forces in pull-out behaviour at such a small scale is very limited. Existing models and theories to describe the pull-out of micro- [27, 28] and nanoscale [19, 24, 29-34] reinforcing materials may not be valid for atomic thin materials. These existing models often consider the frictional type of bonding as the governing force during the pull-out of micro-fibres [27, 28] with a diameter of a few to tens of microns or of nanofibres [20, 35] such as multiwall carbon nanotubes (MWCNTs) which commonly have a diameter in the range tens to hundreds of nanometres [36]. It has been found that at nanometre scale, friction also follows the Amontons' First Law: being proportional to normal force and being a result of surface roughness or, in other words, asperities [37]. However, the question as to whether the friction governed pull-out mechanism can be applied to ATMs (with thickness around or below 1 nm and with correspondingly low surface roughness) has rarely been investigated in the literature. Due to the lack of knowledge about these pull-out mechanisms, there is no existing model to predict reinforcing effects and to provide guidance for the design and fabrication of ATM-reinforced composites.

In this study, the pull-out mechanism of ATMs is investigated to identify the governing forces. On the basis of MD simulation of atomically thin graphene, it is demonstrated that friction is not the dominant force during the pull-out of ATMs. Instead, it is proposed that the pull-out behaviour of ATMs is best described by a constant resistance force (R). The origin of this constant R is the unbalanced adhesion

force between the matrix and the graphene. Based on the unique constant R governing the pull-out process, a new theoretical model is developed to describe the pull-out of 2D ATM. Furthermore, a new formulation of the crack bridging stress is also established for estimation of the reinforcing effect of a 2D ATM such as graphene. Good agreement is found between the model prediction and the reported literature, showing theoretical support for the superior reinforcing efficiency of graphene. The proposed new pull-out mechanism and model provides a way to predict the effects of size, amount and surface properties of atomically thin reinforcements and facilitates the optimal design of future ATM/graphene-reinforced composites.

4.2 Simulation Methods

Molecular dynamics (MD) simulations were conducted to quantify the friction and pull-out interactions between graphene sheet and various matrices. Three types of matrix were used, namely calcium silicate hydrate (C-S-H), aluminium (Al) and polyethylene (PE), which are typical representatives of ceramics/cementitious materials, metals and polymers, respectively. The atomic interaction was modelled by the COMPASS force field (condensed-phased optimized molecular potential for atomistic simulation studies) [38, 39], which is the first *ab initio* force field that was parameterized and validated using condensed-phase properties. This force field has been shown to be applicable in describing the mechanical properties of sp2 carbon [40, 41], calcium silicate hydrate (C-S-H) [42-44], metal [45] and polymers [45-47].

4.2.1 Simulation of Friction

As shown in Figure 4.2-a, a periodic simulation box (49.7 Å x 25.9 Å x 30.8 Å for C-S-H, 88.8 Å x 25.6 Å x 42.5 Å for Al and 42.3 Å x 24.4 Å x 27.0 Å for PE) was created with two layers of matrix materials sandwiching a monolayer graphene (MLG). After

geometry optimization, a 100 ps NPT ensemble (a constant number of particles, constant pressure and temperature dynamics simulation) was employed to optimize the shape of the lattice and relax the system. The pressure was set to be the atmospheric pressure. Then the sheet was assigned a speed v_x and a NVE ensemble (a constant number of particles, constant volume and energy dynamics simulation) was conducted. The speed v_x of all the atoms in the MLG was then extracted under different sliding distances δ. Based on v_x, the loss of global kinetic energy ($\Delta E_{kinetic}$) of the MLG during sliding was computed as

$$\Delta E_{kinetic} = \frac{1}{2} m\left(v_x{}^2(\delta) - v_x{}^2(\delta_0)\right) \tag{4.1}$$

where $v_x(\delta_0)$ is the average speed of all the atoms of MLG after being assigned an initial speed, $v_x(\delta)$ is the average speed of all the atoms of MLG after sliding and m is the mass of the MLG.

The friction force f was then calculated as:

$$f = \frac{\Delta E_{kinetic}}{\delta} \tag{4.2}$$

The interfacial shear strength τ could be given by:

$$\tau = \frac{f}{A} \tag{4.3}$$

where A is the area of MLG.

4.2.2 Simulation of Pull-out

For the simulation of pull-out, a similar sandwiched periodic structure was built in as the simulation of friction, but an isolated MLG (IMLG) sheet was used instead of a continuous MLG sheet, as shown in Figure 4.3-a, d, g and i. Geometry optimization and a 100 ps NPT ensemble at 298 K with atmospheric pressure were employed to optimize the parameter of the simulation box (lattice) and relax the system. To leave

space for the IMLG pull-out, a vacuum gap was introduced in the pull-out direction, while keeping the optimized lattice parameter in the other two directions unchanged. Then the pull-out displacement δ was increased step by step and in each step (including when $\delta = 0$), a 100 ps NVT ensemble (a constant number of particles, constant volume and temperature dynamics simulation) at 298 K was employed to relax the system. On the basis of the relaxed structure, the forces acting on the atoms in the IMLG in the x direction (F_x) applied by the matrices were computed. The interaction energy E_I between matrix and sheet could be calculated as:

$$E_I = E_{total} - (E_{matrix} + E_{sheet}) \tag{4.4}$$

where E_{total} is the total energy of the composite system; E_{matrix} and E_{sheet} are the energies of the matrix and sheet, respectively. By calculating the difference between E_I at the initial state ($\delta = 0$) and at the pulled out state ($\delta > 0$), the corresponding pull-out energy for each step was calculated.

4.3 Pull-out at Atomic Scale

4.3.1 Validation of Friction Governed Pull-out

Micro- and nano-fibre pull-out, with diameters from tens of microns down to tens of nanometres, are considered as friction governed processes (C. Li, 1992, Chen et al., 2014). As shown in Figure 4.1-a, when those fibres are pulled out from the matrix, the abrasion or wear of the surface micro convexities or asperities (red in Figure 4.1-a) causes a frictional resistant force (Sung and Suh, 1979, Dangsheng, 2005). The energy conservation in this case is mainly a balance between the work done by the pull-out force and the energy consumed in bond breaking/reformation (Zhandarov and Mäder, 2005) and agitation of atom movement at the friction interface.

However, when the material is atomically thin with very low surface roughness, such as the graphene shown in Figure 4.1-b, the friction caused by abrasion and wear is substantially reduced. MD simulations were conducted to evaluate the friction level between MLG and various matrices. As in the example of the simulated system shown in Figure 4.2-a, the MLG has a sliding speed v_x and a sliding distance δ. Figure 4.2-b, c and d show the decrease of v_x during sliding in different matrices from δ = 0 to 10 Å due to friction. It can be seen from Figure 4.2-b, c and d that there is an initial sharper drop in v_x within 2 Å for each of three different matrices and after that the rate of decrease of v_x becomes relatively stable.

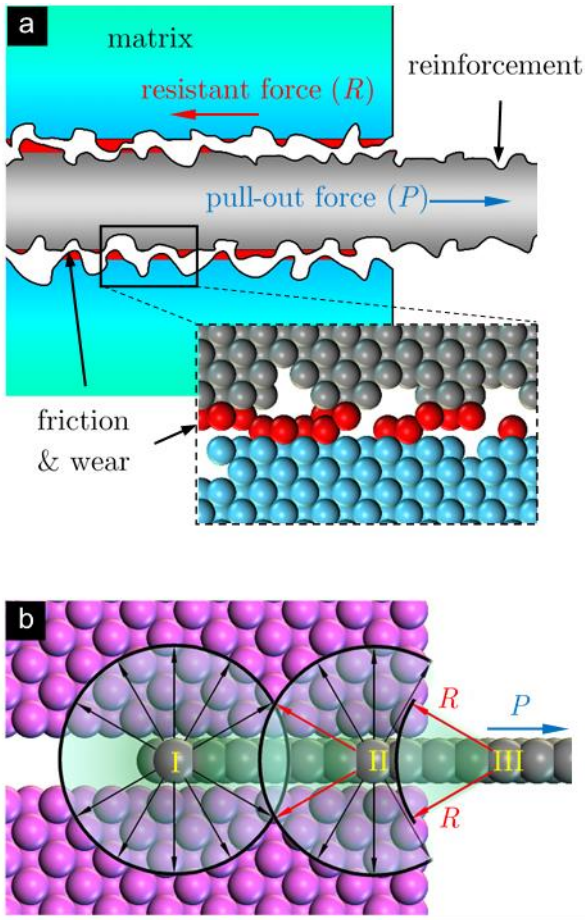

Figure 4.1. Schematics of a) friction governed micro-/nanofibre pull-out (red areas indicate friction-damaged materials during pull-out), and b) adhesion resistance for ATM during pull-out (circles/arcs indicate different force equilibrium at locations I, II and III).

By measuring the decrease of the MLG's speed in the stable stage, the friction force and the interfacial shear strength can be calculated, as shown in Table 4-1. As can be seen, the interfacial shear strength due to friction ranges from 0.13 to 18.71 millipascal. The low friction between the MLG and matrix is consistent with the finding in large scale MD simulation of friction at nanoscale where the friction is caused by nanoscale asperities and a proportional relationship is found between normal pressure and friction force (Mo et al., 2009). The interfacial shear strengths measured here are 9-11 orders of magnitude lower than those derived from the experimental results based on a frictional bond, which are in the range of 18 to 135 MPa (Coleman et al., 2006).

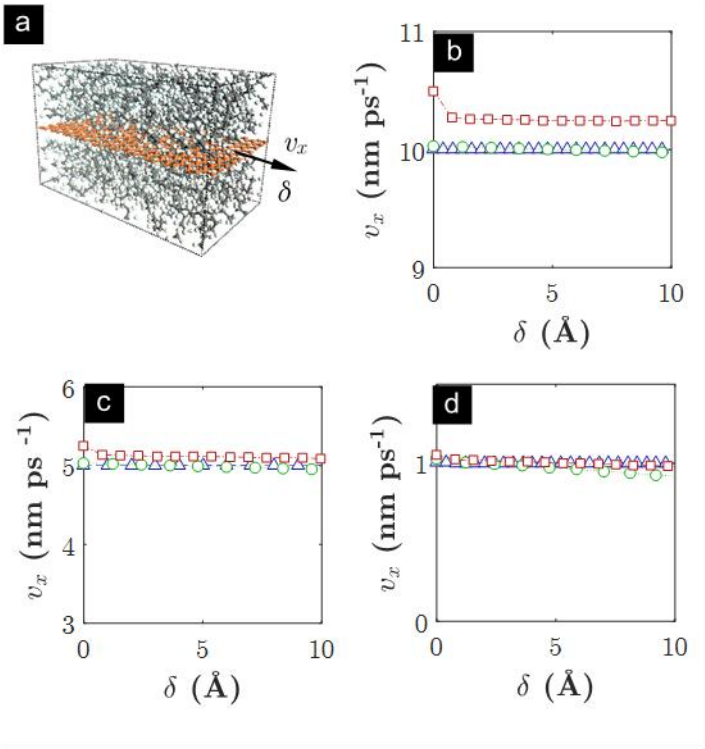

Figure 4.2. (a) Snapshot of a sliding graphene in a periodic simulation box with PE matrix and the decrease of speed of due to friction in b) C-S-H (△), c) metal (○) and d) polymer (□) matrices.

Table 4-1. Decreasing rate of velocity and computed friction coefficient.

Matrix	Initial sliding speed (km/s)	Friction force (zN)	Interfacial shear strength (10^{-3}Pa)
C-S-H	10	21.76	1.69 (±0.02*)

C-S-H	5	16.34	1.27 (±0.06)
C-S-H	1	1.64	0.13(±0.00)
Al	10	426.18	18.71(±0.17)
Al	5	303.04	13.30(±0.15)
Al	1	79.00	3.47(±0.03)
PE	10	119.98	11.64(±0.19)
PE	5	89.47	8.68(±0.09)
PE	1	17.55	1.70(±0.00)

* standard deviation

4.3.2 Governing Forces at Atomic Level: Crack Plane Adhesion

The low level of sliding friction measured in the MD simulations indicated that the frictional bonding based interfacial interaction model was no longer valid. Therefore, non-frictional interaction needed to be considered as the governing mechanism during the pullout of ATMs in order to explain the significant increase in fracture resistance in various matrices (Fan et al., 2010, Liang et al., 2009, Wang et al., 2012a, Porwal et al., 2013).

It is proposed here that the pull-out resistance force (R) for ATM is governed by a different source of forces. As shown in Figure 4.1-b, a monolayer sheet is pulled out from the matrix. For atoms that are distant from the exit, such as atom I, adhesion forces act on them from all directions. For atoms that are close to the crack plane (or fracture surface) of the matrix, however, such as atoms II and III, due to the absence of matrix atoms beyond the crack plane, the adhesion force in those directions disappears. As shown in Figure 4.1-b, the resultant adhesion near the exit is in the opposite direction to the pull-out. Since this adhesion applies only to atoms near the crack plane, it is defined as “crack plane adhesion”. This generates the resistance force R. For ATMs with unit width, this R is theoretically constant during pull-out, regardless of the embedded length of the matrix.

To demonstrate and validate the "crack plane adhesion" phenomenon, force analyses were conducted to analyse the forces on an IMLG applied by the matrix. The forces on each atom of the IMLG in the x direction (F_x) were computed and the distributions of F_x for different matrices and different pull-out distance are shown in Figure 4.3-c, f, h and j. As can be seen, in the part of the IMLG that is distant from the exit region, the positive and negative forces usually appear in pairs and show a pattern in that they can balance each other. In the exit region, however, most atoms have a negative force, forming an adhesion band (ADB). Figure 4.3-a and d show the accumulation of F_x over x. It can be seen that, for the part outside the ADB, the force summation is close to zero and only in the ADB does the force summation begin to decrease to negative. Likewise, such calculations were conducted for IMLGs with Al (Figure 4.3-g) and PE matrix (Figure 4.3-i), where similar phenomenon were found. The magnitude of the crack plane adhesion force (0.27 N/m for C-S-H, 0.88 N/m for Al and 0.50 N/m for PE) is shown to be 10^8-10^9 greater than the friction when the IMLG is around 1 by 1 micron in size. The results here show that the constant R for ATM is dominated by the crack plane adhesion within the ADB.

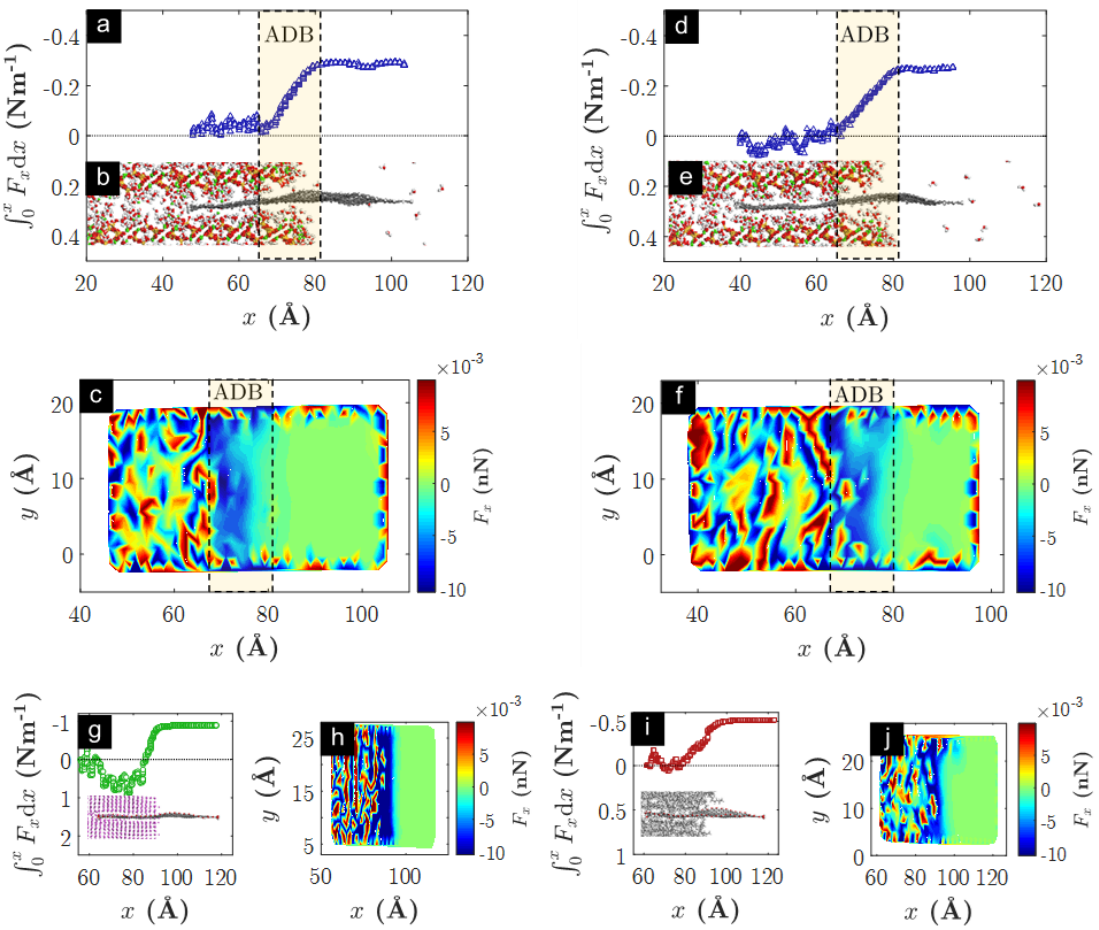

Figure 4.3 Forces on atoms in IMLG in x direction F_x (c, f, h and j) and cumulative F_x (a, d, g and i) applied by the matrix when the IMLG is (a and c) half pull-out and (b and f) ¾ embedded in a C-S-H matrix (△) and half embedded in (g and h) Al (○) and (i and j) PE (□) matrix. (b) and (e) show snapshots of the MD model at the corresponding pull-out distances.

Factors that affect the magnitude of R were also investigated, including matrix material and different sizes of the IMLG (C-S-H: Figure 4.4-a and d, Al: Figure 4.4-b and PE: Figure 4.4-c) and functionalization of IMLG (Figure 4.4-d). Figure 4.4 (e-l) shows the crack plane adhesion governed pull-out energy $E_{p,\,ad}$ and $dE_{p,\,ad}/d\delta$ against δ during different pull-out situations. $dE_{p,\,ad}/d\delta$ equals the pull-out force. As indicated in Figure 4.4-e and f, the different length of the IMLG has no effect on $E_{p,\,ad}$ which increases in an approximately linear manner (constant $dE_{p,\,ad}/d\delta$) except at the very beginning and the end of the pull-out. Figure 4.4-g indicates that doubling the width

also doubles $E_{p,\,ad}$ and $dE_{p,\,ad}/d\delta$. The type of matrix produces the most significance differences in $E_{p,\,ad}$ and $dE_{p,\,ad}/d\delta$ with Al being the highest following by PE and C-S-H (Figure 4.4-e, i and j). In addition, functionalization of the IMLG, which introduces charges and electrostatic attractions between the IMLG and the matrix, increases the magnitude of $E_{p,\,ad}$ and $dE_{p,\,ad}/d\delta$ as shown in Figure 4.4-k and l. The size of the crystal unit cell, or in other words the uniformity of atom distribution, in the matrix is shown to affect the variation of $dE_{p,\,ad}/d\delta$ as the C-S-H (with the most heterogeneous atom distribution) gives the greatest variation of $dE_{p,\,ad}/d\delta$, while Al (with the least heterogeneous atom distribution) gives the smallest. This is because the adhesion forces as illustrated in Figure 4.2-b may not be identical from different directions at nanometre scale due to the non-uniform and non-continuous spatial distribution of atoms in the matrix. However, at a larger scale, such as for graphene length >10 nm, $dE_{p,\,ad}/d\delta$ and R can be treated as statistically constant with only local variations.

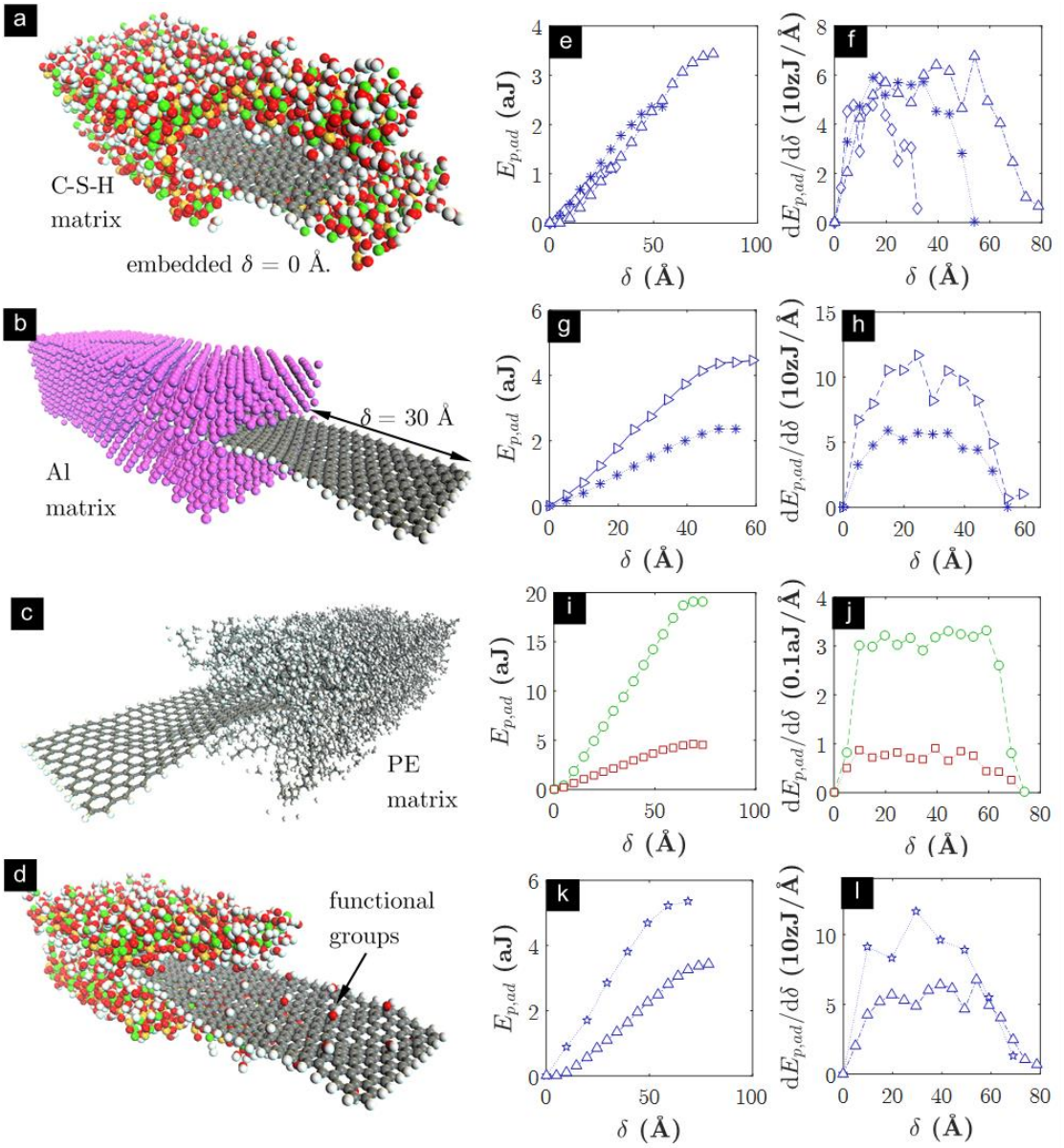

Figure 4.4 Snapshot of pull-out of a monolayer graphene from b) metallic (Al), c) polymeric (PE), and a) and d) cementitious matrices (C-S-H) and (e, g, i and k) $E_{p,ad}$ and (f, h, j and l) changing rate of $E_{p,ad}$ against δ for 20×20* Å (◇), 40×20 Å(∗), 60×20 Å(△), 40×40 Å(▷) graphene and 60×20 Å functionalised graphene (☆) pull-out from C-S-H matrix and 60×20 Å graphene pull-out from Al (○) and PE (□) matrix. Parts of the matrices in (a) and (d) are made invisible to show the embedded part of the graphene sheet. *the dimensions of the sheet are indicated as length × width, with length is in the pull-out direction.

4.3.3 A New Model for the Reinforcing Effect of 2D ATM

Based on the "crack plane adhesion" and constant R theory as given above, a new formulization can be developed to describe the pull-out of 2D ATMs. First, the relations

between the pull-out force P and the pull-out displacement δ for ATMs is established in analogy to the micromechanical model of Li (Lin et al., 1999) for 1D fibres. As shown in Figure 4.5-a, consider a section of atomically thin sheet with infinitesimal width dw, thickness t and initial embedded length L_e. The pull-out process can be separated into two stages: a debonding stage and a debonded stage. During the debonding stage, only for the part within L, the chemical bond between the sheet and the matrix breaks and the part is under tension. dP is the integral of forces along x from 0 to L. The relationship between pull-out force dP and pull-out displacement δ during the debonding stage can be given as (see Appendix A the detailed derivations):

$$\mathrm{d}P = \sqrt{(4G_d + Ct)tE}\ \mathrm{d}w,\ \delta < \delta_0 \tag{4.5}$$

where E is the elastic modulus of the sheet, $C = \dfrac{R}{t\,\mathrm{d}w}$ is the stress as a result of the constant R, G_d is the chemical bond strength, $\delta_0 = \dfrac{\sigma - C}{E} L_e$ corresponds to the displacement at which the sheet is fully debonded, $\sigma = \dfrac{\mathrm{d}P}{t\,\mathrm{d}w}$. As the pull-out displacement δ increases, the sheet and the matrix keep debonding until eventually all the chemical bondings between the sheet and the matrix are broken, giving the debonded stage:

$$\mathrm{d}P = tC\,\mathrm{d}w,\ \delta \geq \delta_0 . \tag{4.6}$$

The relationship between dP and δ was used to derive a new model for the crack bridging stress (σ_B) of ATM embedded in a matrix. σ_B, which indicates the stress that closes the crack during crack propagation, is a measure of the reinforcing effect and reflects the post-cracking strength improvement in the macro sense. Assuming the volume fraction of the ATM is V_{re}, the sheet is a circular flat disk with radius r and the

ATM sheets are 3D randomly located and oriented in the matrix, the new model for σ_B of 2D ATMs is developed (see Appendix B for detailed derivation). As shown in Figure 4.5-b, the *x'* is perpendicular to the opening crack planes I and II. The angle between the ATM/graphene and *x'* is φ. As δ increases, the part of ATM/graphene to the left of plane II (or the upper side in Figure 4.5-c) is pulled out and the part to the right of plane II (or the lower side in Figure 4.5-c) remains embedded. During the pull-out, as shown in Figure 4.5-c, the distance from the center of the ATM/graphene to plane II is *z*. As suggested in Eqs. (1) and (2), *P* is a function of *w* only. Therefore the width *w'* (when $\delta = 0$, $w' = w$) of the ATM/graphene at crack-opening plane I affects the pull-out force on the ATM/graphene (*P*). According to the magnitude of δ compared to δ_0, *w'* can be divided into two parts: a debonded width w'-w_d' and a debonding width w_d'. The pull-out force of the debonding and debonded part is subjected to:

$$P(\delta) = w_d\sqrt{4(G_d + Ct)tE_f} + (w' - w_d)tC \tag{4.7}$$

where $w_d = 2\sqrt{r^2 - (\frac{\delta}{k} + \frac{z}{\cos\phi})^2}$,

$w' - w_d = 2\left(\sqrt{r^2 - (\delta + \frac{z}{\cos\phi})^2} - \sqrt{r^2 - (\frac{\delta}{k} + \frac{z}{\cos\phi})^2}\right)$. When $w_d \le 0$ or $w' \le 0$,

they should be treated as 0, indicating that the sheet is fully debonded or fully pulled out. The bridging stress can be computed as the integration of $P(\delta)$ over different ϕ and *z*:

$$\sigma_B(\delta) = \frac{2V_{re}}{\pi rt}\int_{\phi=0}^{\pi/2}\int_{z=0}^{(r-\delta)\cos\phi} P(\delta)\,p(\phi)\,p(z)\,dz\,d\phi \tag{4.8}$$

where $p(\phi)$ and $p(z)$ are the probability density functions of ϕ and *z* respectively.

Figure 4.5-d demonstrates the variation of σ_B against various parameters including *C*, G_d and *r*. It is evident that the peak of σ_B is at $\delta = 0$ and it increases with G_d and *C*.

The red curves, where $C = 0$ and there is no crack plane adhesion, shows no bridging stress after 10^2 nm. It is interesting to see that due to the constant nature of the crack plane adhesion, the magnitude of r does not affect the peak of σ_B, a feature that is different from friction based models (Chen et al., 2014). However, increasing r does extend the range of σ_B to larger δ (pull distance/crack opening) and thus significantly improves the capability of ATMs to increase fracture energy (increased fracture energy $= \int_0^{+\infty} \sigma_B \, \mathrm{d}\delta$). In Figure 4.5-d, the model predicts the crack bridging stress in the Al matrix with a weight fraction of 0.3% (C = 2.3 GPa, G_d = 0.06 J/m^2, r =1.5 microns and E = 0.5 TPa) as 90 MPa, which is in agreement with the experimentally observed high tensile strength improvement using graphene (95 MPa with inclusion of 0.3 wt% graphene) in Al (Wang et al., 2012a). These results, based on the new model for 2D ATMs, indicate that graphene is a more effective reinforcing material than the 1D MWCNT fibres since about 5-30 times more MWCNTs are required to achieve the same level of crack bridging stress (Chen et al., 2014). This conclusion is also consistent with the reported experimental results of MWCNT reinforcement in Al where about 3.25 wt% MWCNTs are required to achieve a tensile strength improvement of 109 MPa (Kwon et al., 2009). In chapter 5, the crack bridging stress of GO-reinforced cement mortar is estimated and used in the finite element simulation using microplane model.

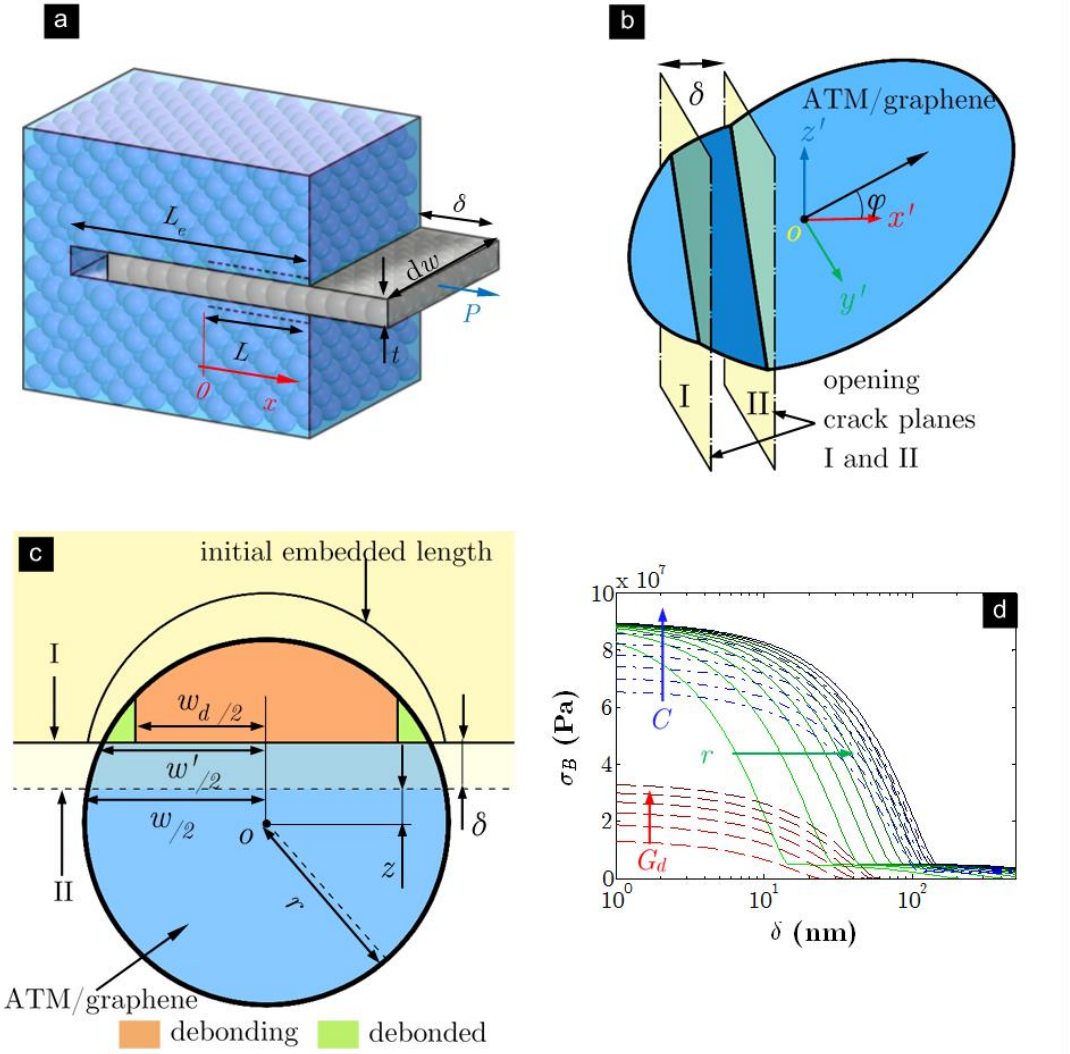

Figure 4.5 a) pull-out model of a section of an ATM sheet with infinitesimal width, b) randomly oriented disk model in 3D space, c) demonstration of debonding and debonded parts during pull-out and d) σ_B vs δ where red, blue and green curves and arrows indicate the effect of increasing G_d, C and r respectively.

4.4 Conclusions

MD simulations were conducted to evaluate the friction level between ATMs and different matrices. It was found that the interfacial shear strength for ATMs, which lack asperities, ranged from 0.13 to 18.71 millipascal and was 9-11 orders of magnitude lower than that derived from experiments.

The unbalanced adhesion around the exit ("crack plane adhesion") results in a constant resistance force, R, and explains the significant enhancing effect of ATMs. Analyses of the forces on an IMLG applied by the matrix validated the constant R theory and an ADB was found within which the constant R originated. MD simulations were conducted to investigate the factors affecting the magnitude of R. It was found that the magnitude of R was irrelevant to the embedded length but proportional to the embedded width. Functionalization of the IMLG also increased the magnitude of R.

Formulization of the relations between the pull-out force and the pull-out displacement for ATMs with infinitesimal width was undertaken. The derived relations could be separated into a debonding stage and a debonded stage. A new theoretical model was developed and could be used to estimate the crack bridging stress (σ_B) for 2D ATM reinforced composites. The ATM sheets were modelled as a circular flat disk and all the sheets were 3D randomly distributed and oriented. According to the derived model, the crack bridging stress of graphene/Al composite was estimated as 95 MPa, which was in agreement with the experimentally observed result. The results demonstrated from a theoretical angle that graphene could be the most efficient reinforcing material, producing 5-30 times more strength improvement than MWCNTs.

In chapter 5, the crack bridging stress of GO reinforced cement mortar is estimated and used in the finite element simulation using microplane model.

CHAPTER 5. FINITE ELEMENT SIMULATIONS USING MICROPLANE MODEL

5.1 Introduction

In this chapter, finite element simulations for static and SHPB tests using the microplane model are presented. As suggested in the literature review, the microplane model develops its macroscopic stress-strain relationships from the mechanics of the microstructure (Babu et al., 2005). The model is promising in the simulation of GO-reinforced cement-based composites, for which the interactions between the reinforcements and the matrix are in the scale of micro- or even nano-level. The up-to-date microplane model M7 (Caner and Bažant, 2012) was coded as a VUMAT user material subroutine and then used in the commercial software suite *ABAQUS (6.13)* to conduct finite element simulations.

First, before the simulation of static and SHPB tests using the microplane model, a comparative study was conducted to compare the microplane model with the widely used concrete damaged plasticity (CDP) model, by which the robustness of the microplane model for the simulation of cement-based materials was examined. The CDP model, as indicated in the literature review, is a representative of the classical approach of the constitutive modelling of cement-based materials, in which the material model is formulated directly in terms of stress and strain tensors and their invariants and cannot capture the interactions of cement-based materials at microscale (Bazant et al., 2000b). The CDP model—with the yield function proposed by Lubliner et al. (1989), and modified by Lee and Fenves (1998) to account for different evolutions of strength under tension and compression, as well as a nonassociated flow rule—is widely accepted and implemented in *ABAQUS (6.13)*. For the comparative study, finite

element simulations of the testing of a three-point bending concrete beam with an asymmetrical notch were revisited by the microplane model and compared with the CDP model results.

After the comparative study, finite element simulations were conducted to simulate the static and SHPB compression tests in Chapter 3 using the microplane model. For the simulations of both the static and SHPB tests, the tests of plain cement mortar were first simulated. Then by adopting the calculated crack bridging stress into the microplane model, the behaviours of GO-reinforced cement mortar were simulated.

5.2 Comparative Study of Microplane Model and Concrete Damaged Plasticity Model

5.2.1 Finite Element Model

Figure 5.1-a shows the geometry, loading and boundary conditions of the three-point bending concrete beam with an asymmetrical notch. The beam had depth D = 75 mm and width 50 mm. The length L of the beam was 340mm, which approximately equalled 9D/2 (Gálvez et al., 1998). The 2mm wide notch reached the depth of 0.5D and was located 37.5mm (D/2) from the support E and 150mm (2D) from the support F. A simply-supported boundary condition was set for the beam. The loading was located at a distance of 84.98mm (1.13D) to the right of the notch.

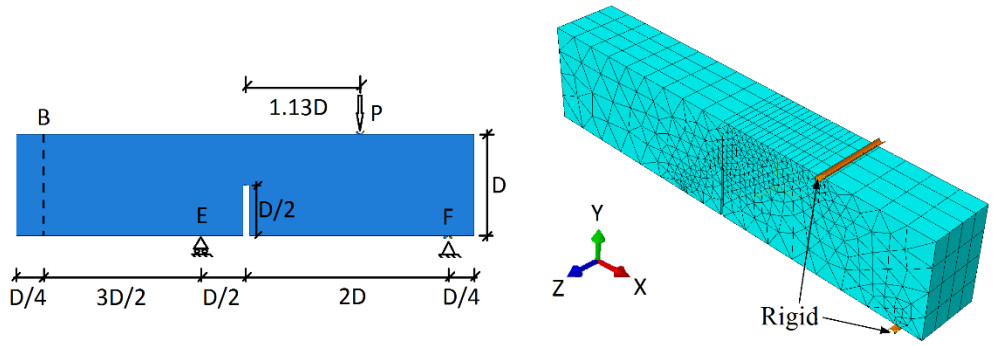

(a) (b)

Figure 5.1 (a) geometry, loading and boundary conditions; (b) finite element mesh

The finite element mesh of the model is presented in Figure 5.1 (b). A simply-supported boundary condition was set on the support E (Ux=0,Uy=0). For the support F and the loading position, two rigid round tubes, which had hard contact (hard contact means that the surfaces transmit no contact pressure unless the surfaces contact each other) with the beam, were placed to simulate the experimental setup. The rigid round tube at support E was fixed and a displacement based loading was applied on the loading rigid round tube.

Three element types, hexahedron (hex), tetrahedron (tet) and wedge, were tried and tested. With the hex element, the crack propagation path was along the notch direction, which disagreed with the experimental finding. With the tet element, although it worked for M7, when used in CDP, the model suffered from excessive distortion of elements, leading to unrealistic deformation of the beam. The wedge element, which worked for both models, was therefore selected in the simulations. As shown in Figure 5.1-b, the finite element size around the predicted crack area was set to be 5mm, as specified in Bazant (2013). Total nodes and elements in the mesh were 1785 and 2568, respectively.

An explicit dynamic algorithm was adopted with a time period of 300s, which could well simulate the static loading process. A mass scaling factor of 1000 was adopted for the whole model to complete the simulation within an acceptable time. Meanwhile, the kinetic energy was monitored to ensure that the ratio of kinetic energy to internal energy was well below 10%, which guaranteed the validity of the simulations when using mass scaling.

5.2.2 Single Point Simulation for Parameters Calibration

To compare the effectiveness of the M7 and CDP models, it must be ensured that the stress-strain relations of both models are similar. Single-point simulations, which directly reflected the stress-strain relations and excluded the influence of boundary conditions, were conducted to calibrate the stress-strain relations of CDP towards M7.

For M7, the Young's modulus and five free model parameters were defined based on Bazant (2013): E = 38,000 MPa, $k_1 = 110 \cdot 10^{-6}$, $k_2 = 110$, $k_3 = 30$, $k_4 = 100$, and $k_5 = 1 \cdot 10^{-4}$.

The calibration was conducted through single point simulations under uniaxial tension and compression. The calibrated parameters of compressive and tensile behaviour in the CDP model are listed in Table 5-1. The other parameters, such as dilation angle $\varphi = 15$, eccentricity $\varepsilon = 0.1$, ratio of the biaxial compression strength to uniaxial compression strength of concrete $\sigma_{b0}/\sigma_{c0} = 1.16$, the ratio of the second stress invariant on the tensile meridian to that on the compressive meridian $K_c = 0.6667$, viscosity parameter $\mu = 0.0$, were default values in *ABAQUS*.

Table 5-1 Parameters of compressive and tensile behaviour in CDP model

Compressive Behaviour	Tensile Behaviour

Inelastic Strain	Yield Stress (MPa)	Damage Parameter	Cracking Strain	Yield Stress (MPa)	Damage Parameter
0	54.043	0	0	4.486	0
0.0004	65.718	0.13	0.0002	3.672	0.3
0.0008	71.345	0.24	0.0006	2.805	0.55
0.0016	72.806	0.34	0.0008	2.419	0.7
0.0024	71.478	0.43	0.0010	2.016	0.8
0.0032	68.353	0.50	0.0016	1.486	0.9
0.0048	64.141	0.57	0.0020	1.221	0.93
0.0128	49.291	0.71	0.0040	0.730	0.95
0.0224	33.518	0.82	0.0060	0.368	0.97
0.0500	15.000	0.97	0.0100	0.302	0.98
0.1000	10.000	0.99	0.0300	0.040	0.99

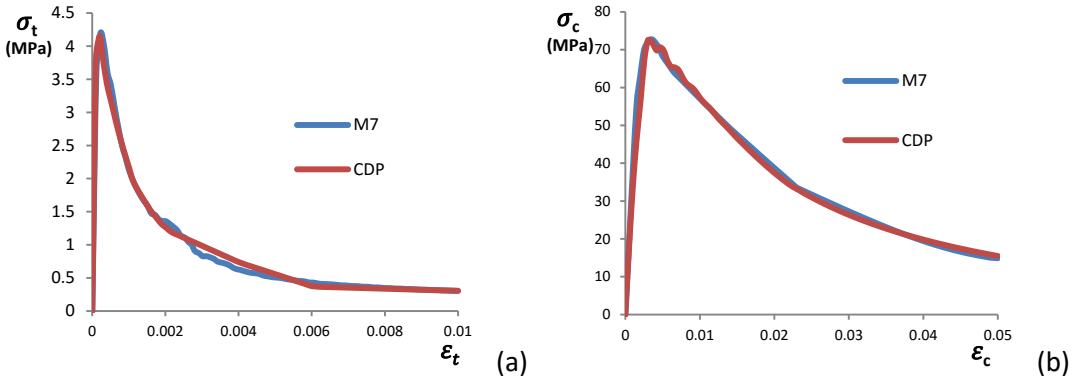

Figure 5.2 Calibration of stress-strain relation under uniaxial tension and compression

Figure 5.2-a and Figure 5.2-b show the calibration of stress-strain relation under uniaxial tension and compression, respectively. It is evident that the stress-strain relations of M7 and CDP are almost the same. In addition, single-point simulations under equibiaxial tension and compression were conducted. The simulation results of equibiaxial tensile strength and compressive strength are shown in Table 5-2. The proximity of the strengths under M7 and CDP further verifies the validity of the calibration.

Table 5-2 Single-point simulation results under equibiaxial tension and compression

Equibiaxial tensile strength (MPa)		Equibiaxial compressive strength (MPa)	
M7	CDP	M7	CDP
4.413	4.585	84.271	85.052

5.2.3 Results and Discussion

The tests of three-point bending concrete beams with an asymmetrical notch produced combined normal and shear stresses in the vertical crack-tip cross-section. This combination of normal and shear stresses gave birth to the mixed-mode crack propagation of concrete, which has perennially been a challenging problem (Bazant, 2013).

Simulation results of load versus displacement at point B with different models are shown in Figure 5.3. The red dots are the simulation result in Bazant (2013) and the experimental result is shown as grey dots. The green curve indicates the simulation result using M7, which matches well the result in Bazant (2013), thus further confirming the validity of finite element model in this paper. The blue curve indicates the simulation result with CDP. It can be found that, in terms of the pre-peak branch and peak load, the simulation results of both models have very good agreement with the experimental results.

Before the displacement at point B reaches 0.1mm, the curves of M7 and CDP are almost identical, which is the consequence of the stress-strain relation calibration. Then, what happened when the displacement at point B reached 0.1mm, leading to the separation of the two curves? Actually, one feature of M7 is that an element deletion criterion is adopted. The criterion is determined by the threshold tensile strain: once

that is exceeded, the element is deleted. This helps to remove elements that suffer from excessive deformation. The default value for element deletion in M7 is 0.005, which was used in the simulation in Figure 5.4. It was found that, when the displacement at point B reached 0.1mm, the tensile strain of the element at the crack tip exceeded 0.005. Therefore, element deletion began and the deleted element could not hold any stress. In comparison, without the inclusion of a failure criterion, element deletion is not possible in *ABAQUS* for the CDP model, which means that the element will always hold some stress. That is why after the displacement at point B reached 0.1mm, the load of M7 decreased more rapidly than CDP.

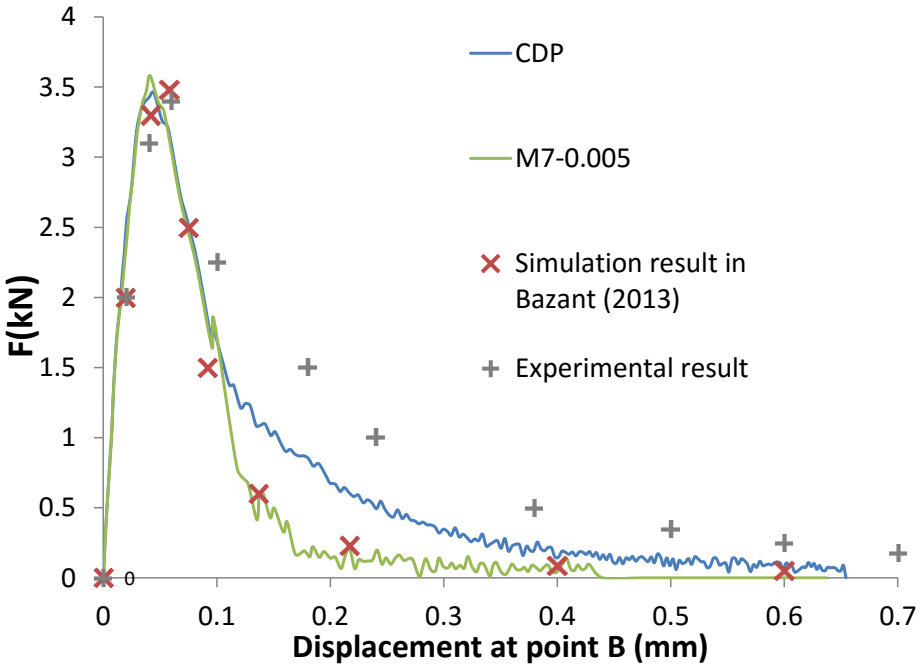

Figure 5.3 Load versus displacement at point B with different models

From Figure 5.3 it can be found that the simulation results of both models fail to give good prediction of the post-peak behaviour of the experimental results. The simulation results underestimate the load in the post-peak branch. However, based on the discussion above, the simulation result of M7 can be calibrated towards the

experiments by changing the threshold value for element deletion. By increasing the threshold value, the element deletion is postponed, which means that the element can hold the stress for a longer time, leading to the increase in the load. Figure 5.4 shows curves of load versus displacement at point B with different element deletion criteria. The red, blue and green curves indicates the threshold values of 0.005, 0.01 and 0.015 respectively. It was found that by increasing the threshold value, the simulation curves had better agreement with the experiments and the curve with the threshold value of 0.015 gave the best prediction.

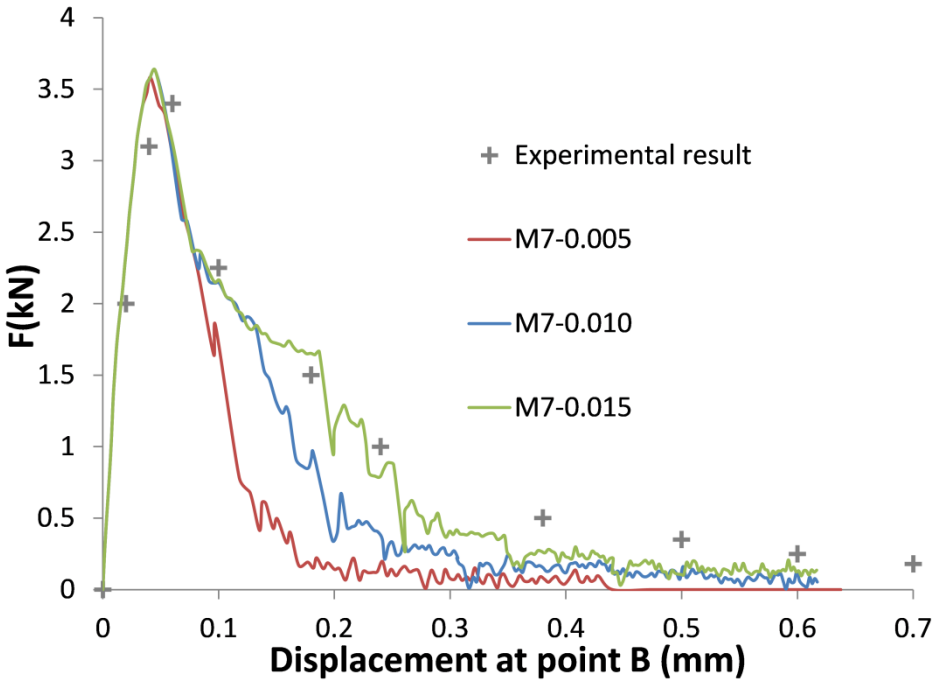

Figure 5.4 Load versus displacement at point B with different element deletion criteria in M7 model

5.3 Numerical Simulations of Static and SHPB Tests Using Microplane Model

5.3.1 Simulations of Static Compression Test

The static compression test was first simulated by the finite element method in *ABAQUS* using the microplane model to validate the crack bridging stress calculated

based on the new crack bridging model proposed in Chapter 4. The finite element model was built as shown in Figure 5.5. The size of the cylinder specimen in the simulation was Ø23.5mm x 47mm, the same as that in the experiments. Then a loading rate of 0.2mm/min, which was also the same as that in the experiments, was assigned to the top plate. The bottom plate was set to be fixed without any displacement.

The microplane model M7 was used as the constitutive model for the specimen. There are five adjustable free parameters from k_1 to k_5 in M7 (Bazant, 2013). These parameters were first calibrated by the simulations for plain cement mortar samples. By adjusting only k_1 to $155 \cdot 10^{-6}$, while keeping the other free parameters the same as their reference values reported by Bazant (2013), the simulation result of the quasi-static compressive strength of the plain cement mortar sample was achieved as 66.2 MPa. The simulation result was approximately the same as the experimental value, indicating good calibration.

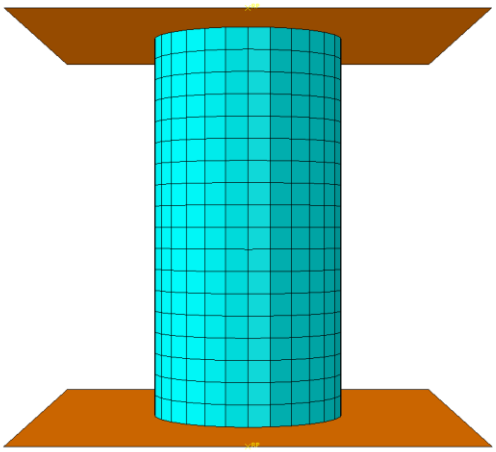

Figure 5.5 Finite element model of quasi-static compressive test

Since M7 was proposed for plain cement-based materials, Caner and Bazant (2013) have modified M7 to M7f to be used for fibre-reinforced cement-based

composites. As indicated in Eq. (5.1), to account for the contributions of the fibres, the microplane normal stress was given by Caner et al. (2013):

$$\sigma_N^{bf} = \sigma_N^b + \sigma_N^f \tag{5.1}$$

where σ_N^{bf} is the total normal boundary for the composites, σ_N^b is the boundary of the matrix and σ_N^f is the contribution from the fibres.

Based on the crack bridging model for 2D ATM reinforced composites proposed in Chapter 4, the crack bridging stress of GO-reinforced cement mortar can be calculated as shown in Figure 5.6. The concentration of GO was 0.2 wt%, with other parameters defined as C = 0.81 GPa, r =1 micron and E = 0.5 TPa, and the chemical bonding was not considered here. By implementing the crack bridging stress as σ_N^f into Eq. 5.1 in the VUMAT subroutine, the static compressive strength of GO-reinforced cement mortar sample was simulated as 75.8 MPa, which was a good approximation of the experimental result (an average of 74 MPa). The good agreement between the simulation and experimental results validated the calculation of the crack bridging stress by the crack bridging model proposed in Chapter 4 and the effectiveness of the microplane model to simulate the static behaviour of GO-reinforced cement-based composites.

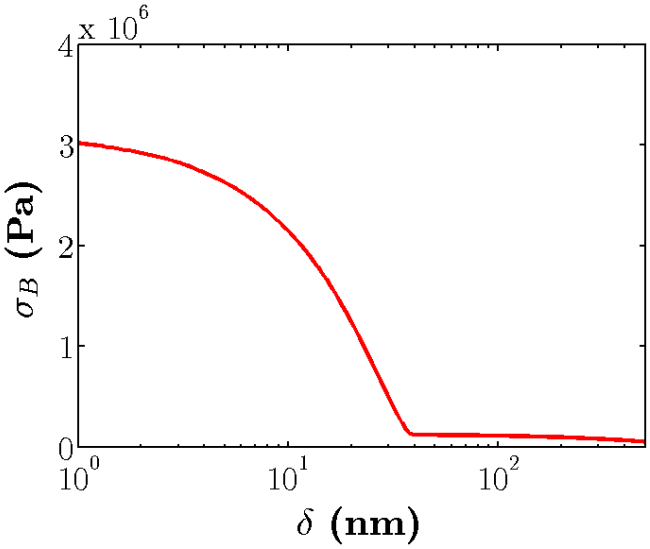

Figure 5.6 Crack bridging stress of GO-reinforced cement mortar

5.3.2 Simulations of SHPB Compression Test

For the simulation of the SHPB test, a 3D model of the entire SHPB testing system was created, as shown in Figure 5.7. The sizes of bars and specimen were same as in the experiments. The aluminium bars were defined as elastic, with Young's modulus 70 GPa and Poisson's ratio 0.3. Spacing of 0.025 mm was set between the interfaces of the specimen and incident/transmitted bar.

A velocity boundary condition was applied on the striker bar. The contact property in the tangential direction between aluminium bars and between bar and specimen was assumed to be frictionless. In the normal direction, the contact properties were defined as an exponential pressure-overclosure relationship, as shown in Table 5-3. The meshes around the interfaces are shown in Figure 5.7. A denser finite element size of 1mm was chosen for the mortar specimen.

Table 5-3 Contact properties in the normal direction of the interfaces

bar-bar interaction		bar-specimen interaction	
Pressure	Clearance	Pressure	Clearance

$5 \cdot 10^8$	0	$2.5 \cdot 10^8$	0
0	$2 \cdot 10^{-4}$	0	$2.5 \cdot 10^{-5}$

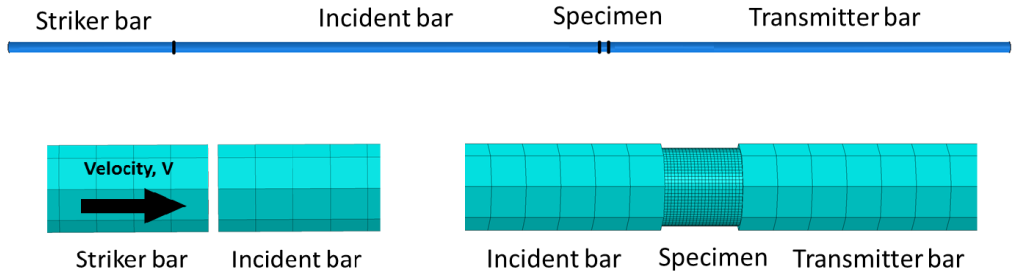

Figure 5.7 Finite element model of SHPB test

The rate effect was introduced in the microplane model in Bazant et al. (2000a). The equation accounting for the rate effect has the form:

$$\sigma(\varepsilon) = \sigma^0(\varepsilon)\left[1 + C_2 a \sinh\left(\frac{\dot{\varepsilon}}{C_1}\right)\right] \tag{5.2}$$

Function $\sigma(\varepsilon)$ represents the static stress-strain boundary (i.e., strain-dependent yield limits) on the microplane without the strain rate effect. Function $\sigma^0(\varepsilon)$ can be interpreted as the stress-strain boundary on the microplane corresponding to strain rate $\dot{\varepsilon}$ and the transformation from the static boundary $\sigma^0(\varepsilon)$ to the rate-dependent (dynamic) boundary $\sigma(\varepsilon)$ represents a vertical scaling of the boundary curve (Caner and Bažant, 2014). C_1 and C_2 are the two adjustable parameters. Actually, if $\dot{\varepsilon} \succ\succ C_1$, Eq. 5.2 can be simplified (Bazant et al., 2000a) as:

$$\sigma(\varepsilon) = \sigma^0(\varepsilon)\left[1 + C_2 a \sinh\left(\frac{\dot{\varepsilon}}{C_1}\right)\right] \approx \sigma^0(\varepsilon)\left[1 + C_2 \ln\left(\frac{2\dot{\varepsilon}}{C_1}\right)\right] \tag{5.3}$$

If $\frac{\sigma(\varepsilon)}{\sigma^0(\varepsilon)}$ is defined as DIF, then the relation between DIF and the strain rate is a logarithmic relation, which is consistent with the empirical equations for cement-based

materials concluded by many researchers (Tedesco et al., 1993, Zhou and Hao, 2008, Bischoff and Perry, 1991).

First, a normal boundary without crack bridging stress σ_N^b was adopted and subjected to the strain rate effect as indicated in Eq. 5.2. The two strain rate parameters were calibrated as $C_1 = 4 \cdot 10^{-6}$ and $C_2 = 0.016$. As shown in Figure 5.8, the simulation results are represented as red dots. The blue, red and green curve are the best fit for the experimental results of SHPB compressive strength as described in Figure 3.10. Good agreement was achieved between the simulation results and experimental results, indicating the effectiveness of the model for simulating the dynamic response of plain cement mortar samples.

Then, to simulate the dynamic response of GO-reinforced cement mortar, the normal boundary σ_N^{bf} including the crack bridging stress was adopted. The two strain rate parameters C_1 and C_2 were the same as the calibrated values given above. The simulation results were indicated as black dots in Figure 5.8. It can be seen that for the lower strain rate, the simulation results still match the experiments well. But for higher strain rates, the simulation results give a significant underestimation. This finding meant that the current equations with a logarithmic relation between the DIF and strain rate in the microplane model were not suitable for the simulation of GO-reinforced cement-based composites under high strain rate loadings.

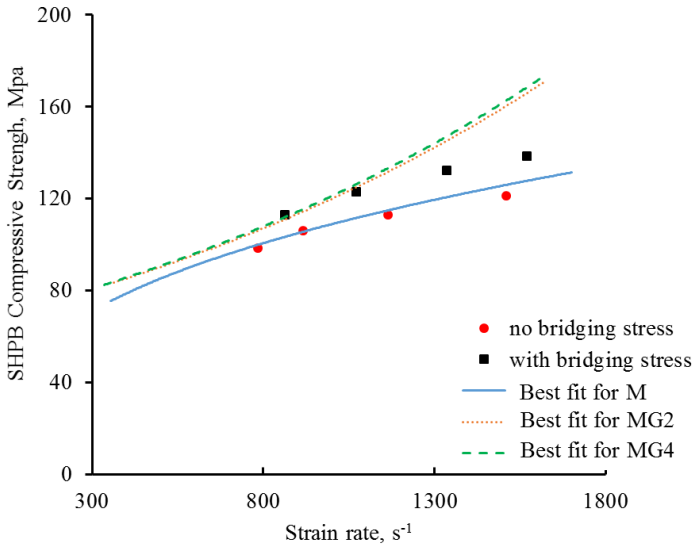

Figure 5.8 Simulation results of SHPB test

5.4 Conclusions

In this chapter, finite element simulations were conducted using the microplane model. From the simulation results, the following conclusions were drawn:

(1) In the comparative study of the static three-point bending test, both M7 and CDP could predict well the ascending branch and the peak load. With an element deletion criterion, M7 gave closer predictions for the descending branch whereas CDP failed to do so, a result which demonstrated the robustness of the M7 model for the simulation of cement-based materials.

(2) In the simulation of the static test, on the basis of the parameters calibrated by the simulation of plain cement mortar, by simply including the calculated crack bridging stress into the normal boundary, the experimental compressive strength of the GO-reinforced cement mortar was accurately simulated. This good agreement validated the calculation of the crack bridging stress by the proposed model in

Chapter 4 and the effectiveness of the microplane model to simulate the static behaviour of GO-reinforced cement-based composites.

(3) In the simulation of the SHPB test, the microplane model with a logarithmic relation between the DIF and the strain rate to account for the strain rate effect worked for the simulation of plain cement mortar samples. However, in simulation of the GO-reinforced mortar samples, the simulation results gave a significant underestimation compared with the experimental results under higher strain rates.

CHAPTER 6. CONCLUSIONS AND RECOMMENDATIONS

6.1 Conclusions

This thesis investigated the reinforcing effect of GO on cement mortar under high strain rate loadings by both experimental and numerical analysis. On the basis of the studies, the following conclusions were obtained:

(1) With the incorporation of GO, static tensile splitting and compressive strength were both improved. SHPB tests showed that both tensile splitting and compressive strength for GO-reinforced cement mortar increased with the increase of strain rate. However, compared with the SHPB tensile splitting tests, in which the DIF of GO-reinforced cement mortar and plain cement mortar were similar under different strain rates, the DIF of GO-reinforced cement mortar for SHPB compression was significantly higher than that of the plain cement mortar at higher strain rate. Analysis of the fragments after SHPB testing showed that in the SHPB compression tests, the cracks were diffused over the entire samples and there was a significant increase in the number of cracks under higher strain rates, creating many more fracture surfaces, which resulted in a higher possibility of cracks passing through the GO nanosheets and producing a more significant reinforcing effect of GO.

(2) On the basis of the MD simulations of ATM pull-out from different matrices, friction was found to make a negligible contribution to the pull-out force because of the lack of asperities on ATM. The pull-out force was revealed to be governed by a “crack plane adhesion”. Unlike frictional pull-out, the crack plane adhesion produces a pull-out force independent of the embedded length of ATM. Based on crack plane adhesion, the relations between the pull-out force and the pull-out

displacement for ATM were formulized. Furthermore, a new theoretical crack bridging model was developed to predict the crack bridging stress (σ_B) for 2D ATM. Based on the material properties and mix design for GO-reinforced cement mortar, the maximum crack bridging stress of GO-reinforced cement mortar was estimated to be 3MPa.

(3) Finite element simulation of the static compression test showed that, by including the calculated crack bridging stress into the normal boundary, the experimental compressive strength of GO-reinforced mortar could be accurately simulated by using the microplane model. This good agreement validated the calculation of the crack bridging stress by the proposed crack bridging model in Chapter 4 and the effectiveness of the microplane model in simulating the static behaviour of GO-reinforced cement-based composites. For the simulation of the SHPB test, the microplane model with a widely adopted empirical logarithmic relation between the DIF and the strain rate to account for the strain rate effect worked for the simulations of plain cement mortar samples. However, in simulations of the GO-reinforced cement mortar samples, the simulation results gave a significant underestimation compared with the experimental results under higher strain rates.

6.2 Recommendations for Future Studies

Based on the findings reported in this thesis, the following recommendation are made for future studies:

(1) This study focused on the mechanical properties of GO-reinforced cement mortar only. Extended research incorporating GO into cement paste or concrete under various loading conditions is necessary for wider applications in civil infrastructure.

(2) The new crack bridging model for ATM reinforced composites proposed in this study made a couple of assumptions to simplify the problem. For example, the shape of all the ATM was simplified as a circular flat disk, but in reality, these materials can have different shapes. The model assumed perfect dispersion of the ATM, but in reality, only part of the ATM is well dispersed. By addressing these problems, the model can be further modified.

(3) SHPB tests and simulations showed that the widely adopted empirical logarithmic relation between DIF and strain rate is not applicable to GO-reinforced cement-based materials. More tests need to be conducted to summarize new empirical equations.

APPENDIX A: DERIVATION OF CRACK PLANE ADHESION GOVERNED PULL-OUT LAW

As shown in Figure 4.5-a, the relations between the pull-out force *P* and the pull-out displacement δ for a section of ATM sheet with infinitesimal width d*w* is derived here. In the debonded region, the following relations can be given based on the equilibrium requirement:

$$\sigma_{re}(x) = \sigma_{re0} \tag{A1}$$

$$\sigma_{m}(x) = \sigma_{m0} \tag{A2}$$

where σ_{re0} and σ_{m0} are the normal stresses in the reinforcing ATM sheet and the matrix respectively at $x = 0$, and they are given by:

$$\sigma_{re(0)} = \sigma - C \tag{A3}$$

$$\sigma_{m0} = \frac{CV_{re}}{V_m} \tag{A4}$$

where V_{re} and V_m are the volume fractions of ATM sheet and matrix respectively.

Define the relative displacement between the sheet and matrix in the debonded region as:

$$\Delta(x) = u_{re}(x) - u_m(x) \tag{A5}$$

Then,

$$\frac{\mathrm{d}\Delta(x)}{\mathrm{d}x} = \frac{\mathrm{d}u_{re}(x)}{\mathrm{d}x} - \frac{\mathrm{d}u_m(x)}{\mathrm{d}x} = \frac{\sigma_{re}(x)}{E} - \frac{\sigma_m(x)}{E_m} = \frac{\sigma_{re0}}{E} - \frac{\sigma_{m0}}{E_m} = \frac{\sigma - C}{E} - \frac{CV_r}{V_m} \tag{A6}$$

where E_m is the elastic modulus of the matrix.

So, we have:

$$\Delta(x) = \int_0^x \frac{\mathrm{d}\Delta(x)}{\mathrm{d}x}\mathrm{d}x = \left(\frac{\sigma - C}{E} - \frac{C\eta}{E}\right)x + C' \tag{A7}$$

where $\eta = \dfrac{V_{re}E}{V_m E_m}$ and $C' = 0$, because $\Delta(x) = 0$ when $x = 0$.

Because $\dfrac{C\eta}{E} \to 0$, the pull-out displacement δ can be given by:

$$\delta = \Delta(L) = \frac{\sigma - C}{E} L \tag{A8}$$

According to energy conservation, for any infinitesimal advance of the debonded region $\mathrm{d}A$,

$$P\,\mathrm{d}u_{re} = \mathrm{d}U + \mathrm{d}W_{re} + G_d\,\mathrm{d}A \tag{A9}$$

where u_{re} is the displacement at the pull-out sheet end; $\mathrm{d}U$ is the strain energy change in the system; $\mathrm{d}W_{re}$ is the change of the energy dissipated by constant R at the interface; $G_d\,\mathrm{d}A$ indicates the energy consumed in the advance of debonded zone.

For any elastic system,

$$\mathrm{d}U = \frac{1}{2}(P\,\mathrm{d}u_{re} - \mathrm{d}W_{re}) \tag{A10}$$

Combining (A10) and (A11):

$$G_d\,\mathrm{d}A = \frac{1}{2}\left(P\,\mathrm{d}u_{re} - \mathrm{d}W_{re}\right) \tag{A11}$$

Because

$$u_{re} = \int_0^L \frac{\sigma_{re}(z)}{E}\,\mathrm{d}z + \frac{V_{re}\sigma}{E_c}(L_e - L) \tag{A12}$$

where $E_c = V_{re}E + V_m E_m$, we have:

$$\mathrm{d}u_{re} = \left(\frac{\sigma}{E} - \frac{V_{re}\sigma}{E_c}\right)\mathrm{d}z \tag{A13}$$

The W_{re} can be obtained by:

$$W_{re} = Ctz\,\mathrm{d}w \tag{A14}$$

In combination with

$$\mathrm{d}P = t\sigma\,\mathrm{d}w \tag{A15}$$

and

$$\mathrm{d}A = 2w\mathrm{d}z \tag{A16}$$

(A12) can be rewritten as:

$$4G_d\,\mathrm{d}w = t\,\mathrm{d}w\sigma^2\frac{1}{E(1+\eta)} - Ct\,\mathrm{d}w \tag{A17}$$

Because $\eta \to 0$, we have:

$$4G_d \,\mathrm{d}w + Ct\,\mathrm{d}w = \frac{t\,\mathrm{d}w\sigma^2}{E} \tag{A18}$$

Finally, the σ and P can be obtained:

$$\sigma = \sqrt{\frac{4G_d + Ct}{t}E} \tag{A19}$$

$$\mathrm{d}P = \sqrt{(4G_d + Ct)tE}\,\mathrm{d}w \tag{A20}$$

When $L = L_e$, the sheet is fully debonded.

So, when $\delta > \delta_0$,

$$\delta_0 = \frac{\sigma - C}{E}L_e \tag{A21}$$

$$\mathrm{d}P = tC\,\mathrm{d}w \tag{A22}$$

APPENDIX B: DERIVATION OF CRACK BRIDGING STRESS

The micromechanical model for 1D fibre reinforced composites of Li (Li et al., 1991) is modified here for 2D ATM sheet to calculate the crack bridging stress. As indicated by (A20) and (A22), the pull-out force of the sheet is in proportion to its width at the interface with the matrix. As shown in Figure 4.5-b and c, to locate a sheet and determine its width at the interface, two parameters are needed: orientation angle ϕ and centroidal distance z. Then the probability density function $p(\phi)$ and $p(z)$ can be given by:

$$p(\phi) = \sin\phi \tag{A23}$$

$$p(z) = \frac{1}{r} \tag{A24}$$

By integrating the pull-out force of all the sheets that cross the crack plane, the relationship between the crack bridging stress σ_B and the pull-out displacement δ can be given by:

$$\sigma_B(\delta) = \frac{2V_{re}}{\pi Rt}\int_{\phi=0}^{\pi/2}\int_{z=0}^{(r-\delta)\cos\phi} P(\delta)\,p(\phi)\,p(z)\,dz\,d\phi \tag{A25}$$

The equation of $P(\delta)$ can be separated into two stages.

When $\delta \prec \delta_0 = k\left(r - \frac{z}{\cos\phi}\right)$, the sheet is partially debonded. The debonding width *wd'* and debonded width can be given by:

$$w_d' = 2\sqrt{r^2 - (\frac{\delta}{k} + \frac{z}{\cos\phi})^2} \tag{A26}$$

$$w' - w_d' = 2\left(\sqrt{r^2 - (\delta + \frac{z}{\cos\phi})^2} - \sqrt{r^2 - (\frac{\delta}{k} + \frac{z}{\cos\phi})^2}\right) \tag{A27}$$

So, the equation of $P(\delta)$ can be obtained:

$$P(\delta)_{partial} = 2\left(\sqrt{r^2 - (\frac{\delta}{k} + \frac{z}{\cos\phi})^2}\right)\sqrt{4(G_d + Ct)tE_f} + 2\left(\sqrt{r^2 - (\delta + \frac{z}{\cos\phi})^2} - \sqrt{r^2 - (\frac{\delta}{k} + \frac{z}{\cos\phi})^2}\right)tc \tag{A28}$$

When $\delta \geq \delta_0 = k\left(r - \frac{z}{\cos\phi}\right)$, there is only the debonded part, so $P(\delta)$ can be given by:

$$P(\delta)_{full} = 2\sqrt{r^2 - (\delta + \frac{z}{\cos\phi})^2}\,tc \qquad \text{(A29)}$$

REFERENCES

ABAQUS 6.13. ABAQUS 6.13. *Analysis User's Guide, Dassault Systems*.

AJAYAN, P. M., SCHADLER, L. S., GIANNARIS, C. & RUBIO, A. 2000. Single-walled carbon nanotube–polymer composites: strength and weakness. *Advanced Materials,* 12**,** 750-753.

AL-OSTAZ, A., WU, W., CHENG, A.-D. & SONG, C. 2010. A molecular dynamics and microporomechanics study on the mechanical properties of major constituents of hydrated cement. *Composites Part B: Engineering,* 41**,** 543-549.

ALLEN, A. J., THOMAS, J. J. & JENNINGS, H. M. 2007. Composition and density of nanoscale calcium–silicate–hydrate in cement. *Nature materials,* 6**,** 311-316.

BABU, R., BENIPAL, G. & SINGH, A. 2005. Constitutive modelling of concrete: an overview. *Asian Jounal of Civil Engineering (Building and Housing),* 6**,** 211-246.

BAGRI, A., MATTEVI, C., ACIK, M., CHABAL, Y. J., CHHOWALLA, M. & SHENOY, V. B. 2010. Structural evolution during the reduction of chemically derived graphene oxide. *Nature chemistry,* 2**,** 581-587.

BAKSHI, S., LAHIRI, D. & AGARWAL, A. 2010. Carbon nanotube reinforced metal matrix composites-a review. *International Materials Reviews,* 55**,** 41-64.

BALAGURU, P. N. & SHAH, S. P. 1992. *Fiber-reinforced cement composites*.

BARADARAN, S., MOGHADDAM, E., BASIRUN, W., MEHRALI, M., SOOKHAKIAN, M., HAMDI, M., MOGHADDAM, M. N. & ALIAS, Y. 2014. Mechanical properties and biomedical applications of a nanotube hydroxyapatite-reduced graphene oxide composite. *Carbon,* 69**,** 32-45.

BAŽANT, Z. 1984. Microplane model for strain controlled inelastic behaviour, Chapter 3. *CS Desai and RH Gallagher eds*.

BAZANT, Z. P. 2010. Can multiscale-multiphysics methods predict softening damage and structural failure? *International Journal for Multiscale Computational Engineering,* 8.

BAZANT, Z. P. 2013. Microplane Model M7 for Plain Concrete. II: Calibration and Verification. *Journal of Engineering Mechanics,* 139**,** 1724-1735.

BAZANT, Z. P., CANER, F. C., ADLEY, M. D. & AKERS, S. A. 2000a. Fracturing rate effect and creep in microplane model for dynamics. *Journal of engineering mechanics,* 126**,** 962-970.

BAZANT, Z. P., CANER, F. C., CAROL, I., ADLEY, M. D. & AKERS, S. A. 2000b. Microplane model M4 for concrete. I: Formulation with work-conjugate deviatoric stress. *Journal of Engineering Mechanics,* 126**,** 944-953.

BENTUR, A. & MINDESS, S. 2006. *Fibre reinforced cementitious composites*, CRC Press.

BISCHOFF, P. & PERRY, S. 1991. Compressive behaviour of concrete at high strain rates. *Materials and structures,* 24**,** 425-450.

BONACCORSI, E., MERLINO, S. & TAYLOR, H. 2004. The crystal structure of jennite, Ca 9 Si 6 O 18 (OH) 6· 8H 2 O. *Cement and Concrete Research,* 34**,** 1481-1488.

BRARA, A. & KLEPACZKO, J. 2006. Experimental characterization of concrete in dynamic tension. *Mechanics of materials,* 38**,** 253-267.

BROCCA, M. & BAZANT, Z. E. K. P. 2001. Size effect in concrete columns: finite-element analysis with microplane model. *Journal of Structural Engineering,* 127**,** 1382-1390.

BROCCA, M. & BAZANT, Z. P. 2000. Microplane constitutive model and metal plasticity. *Applied Mechanics Reviews,* 53**,** 265-281.

BROCCA, M. & BAŽANT, Z. P. 2001. Microplane finite element analysis of tube-squash test of concrete with shear angles up to 70°. *International Journal for Numerical Methods in Engineering,* 52**,** 1165-1188.

BUNTE, S. W. & SUN, H. 2000. Molecular modeling of energetic materials: the parameterization and validation of nitrate esters in the COMPASS force field. *The Journal of Physical Chemistry B,* 104**,** 2477-2489.

C109/C109M-16, A. 2016. Standard Test Method for Compressive Strength of Hydraulic Cement Mortars (Using 2-in. or [50-mm] Cube Specimens). ASTM International West Conshohocken, Pa.

C150, A. 1999. Standard Specification for Portland Cement. ASTM International West Conshohocken, Pa.

C496/C496M-11, A. 2004. Standard Test Method for Splitting Tensile Strength of Cylindrical Concrete Specimens. ASTM International West Conshohocken, Pa.

C1437-15, A. 2015. Standard Test Method for Flow of Hydraulic Cement Mortar. ASTM International West Conshohocken, Pa.

C. LI, V. 1992. Postcrack scaling relations for fiber reinforced cementitious composites. *Journal of Materials in Civil Engineering,* 4**,** 41-57.

CANER, F. C. & BAŽANT, Z. P. 2012. Microplane model M7 for plain concrete. I: Formulation. *Journal of Engineering Mechanics,* 139**,** 1714-1723.

CANER, F. C. & BAŽANT, Z. P. 2014. Impact comminution of solids due to local kinetic energy of high shear strain rate: II–Microplane model and verification. *Journal of the Mechanics and Physics of Solids,* 64**,** 236-248.

CANER, F. C., BAZANT, Z. P. & CERVENKA, J. 2002. Vertex effect in strain-softening concrete at rotating principal axes. *Journal of engineering mechanics,* 128**,** 24-33.

CANER, F. C., BAŽANT, Z. P. & WENDNER, R. 2013. Microplane model M7f for fiber reinforced concrete. *Engineering Fracture Mechanics,* 105**,** 41-57.

CHATTERJEE, S., WANG, J., KUO, W., TAI, N., SALZMANN, C., LI, W., HOLLERTZ, R., NÜESCH, F. & CHU, B. 2012. Mechanical reinforcement and thermal conductivity in expanded graphene nanoplatelets reinforced epoxy composites. *Chemical Physics Letters,* 531**,** 6-10.

CHEN, S., COLLINS, F., MACLEOD, A., PAN, Z., DUAN, W. & WANG, C. 2011. Carbon nanotube–cement composites: A retrospect. *The IES Journal Part A: Civil & Structural Engineering,* 4**,** 254-265.

CHEN, S. J., ZOU, B., COLLINS, F., ZHAO, X. L., MAJUMBER, M. & DUAN, W. H. 2014. Predicting the influence of ultrasonication energy on the reinforcing efficiency of carbon nanotubes. *Carbon,* 77**,** 1-10.

CHUAH, S., PAN, Z., SANJAYAN, J. G., WANG, C. M. & DUAN, W. H. 2014. Nano reinforced cement and concrete composites and new perspective from graphene oxide. *Construction and Building Materials,* 73**,** 113-124.

COLEMAN, J. N., KHAN, U., BLAU, W. J. & GUN'KO, Y. K. 2006. Small but strong: a review of the mechanical properties of carbon nanotube–polymer composites. *Carbon,* 44**,** 1624-1652.

COTSOVOS, D. & PAVLOVIĆ, M. 2008. Numerical investigation of concrete subjected to compressive impact loading. Part 1: A fundamental explanation for the apparent strength gain at high loading rates. *Computers & structures,* 86**,** 145-163.

DANGSHENG, X. 2005. Friction and wear properties of UHMWPE composites reinforced with carbon fiber. *Materials letters,* 59**,** 175-179.

DIKIN, D. A., STANKOVICH, S., ZIMNEY, E. J., PINER, R. D., DOMMETT, G. H., EVMENENKO, G., NGUYEN, S. T. & RUOFF, R. S. 2007. Preparation and characterization of graphene oxide paper. *Nature,* 448**,** 457-460.

DRESSELHAUS, M. S., DRESSELHAUS, G., EKLUND, P. & RAO, A. 2000. *Carbon nanotubes*, Springer.

DUAN, W., WANG, Q., LIEW, K. M. & HE, X. 2007. Molecular mechanics modeling of carbon nanotube fracture. *Carbon,* 45**,** 1769-1776.

DUAN, W. H., GONG, K. & WANG, Q. 2011. Controlling the formation of wrinkles in a single layer graphene sheet subjected to in-plane shear. *Carbon,* 49**,** 3107-3112.
FAN, H., WANG, L., ZHAO, K., LI, N., SHI, Z., GE, Z. & JIN, Z. 2010. Fabrication, mechanical properties, and biocompatibility of graphene-reinforced chitosan composites. *Biomacromolecules,* 11**,** 2345-2351.
FENG, K. N., RUAN, D., PAN, Z., COLLINS, F., BAI, Y., WANG, C. M. & DUAN, W. H. 2014. Effect of strain rate on splitting tensile strength of geopolymer concrete. *Magazine of Concrete Research,* 66**,** 825-835.
FIELD, J., WALLEY, S., PROUD, W., GOLDREIN, H. & SIVIOUR, C. 2004. Review of experimental techniques for high rate deformation and shock studies. *International Journal of Impact Engineering,* 30**,** 725-775.
GÁLVEZ, J., ELICES, M., GUINEA, G. & PLANAS, J. 1998. Mixed mode fracture of concrete under proportional and nonproportional loading. *International Journal of Fracture,* 94**,** 267-284.
GIACCIO, G. & ZERBINO, R. 1998. Failure mechanism of concrete: combined effects of coarse aggregates and strength level. *Advanced Cement Based Materials,* 7**,** 41-48.
GONG, K., PAN, Z., KORAYEM, A. H., QIU, L., LI, D., COLLINS, F., WANG, C. M. & DUAN, W. H. 2014. Reinforcing effects of graphene oxide on portland cement paste. *Journal of Materials in Civil Engineering,* 27**,** A4014010.
GOU, J., MINAIE, B., WANG, B., LIANG, Z. & ZHANG, C. 2004. Computational and experimental study of interfacial bonding of single-walled nanotube reinforced composites. *Computational Materials Science,* 31**,** 225-236.
HARRISON, B. S. & ATALA, A. 2007. Carbon nanotube applications for tissue engineering. *Biomaterials,* 28**,** 344-353.
HOPKINSON, J. 1872. On the rupture of iron wire by a blow. *Manchester Literary and Philosophical Society,* 11**,** 40-45.
HOU, D. & LI, Z. 2013. Molecular dynamics study of water and ions transported during the nanopore calcium silicate phase: case study of jennite. *Journal of materials in civil engineering,* 26**,** 930-940.
HOU, D., ZHU, Y., LU, Y. & LI, Z. 2014. Mechanical properties of calcium silicate hydrate (C–S–H) at nano-scale: a molecular dynamics study. *Materials Chemistry and Physics,* 146**,** 503-511.
HSUEH, C.-H. 1990. Interfacial debonding and fiber pull-out stresses of fiber-reinforced composites. *Materials Science and Engineering: A,* 123**,** 1-11.
HWANG, J., YOON, T., JIN, S. H., LEE, J., KIM, T. S., HONG, S. H. & JEON, S. 2013. Enhanced Mechanical Properties of Graphene/Copper Nanocomposites Using a Molecular-Level Mixing Process. *Advanced Materials,* 25**,** 6724-6729.
ISTRATE, O. M., PATON, K. R., KHAN, U., O'NEILL, A., BELL, A. P. & COLEMAN, J. N. 2014. Reinforcement in melt-processed polymer–graphene composites at extremely low graphene loading level. *Carbon,* 78**,** 243-249.
KIM, W., LEE, T. & HAN, S. 2014. Multi-layer graphene/copper composites: Preparation using high-ratio differential speed rolling, microstructure and mechanical properties. *Carbon,* 69**,** 55-65.
KOLSKY, H. 1949. An investigation of the mechanical properties of materials at very high rates of loading. *Proceedings of the Physical Society. Section B,* 62**,** 676.
KWON, H., ESTILI, M., TAKAGI, K., MIYAZAKI, T. & KAWASAKI, A. 2009. Combination of hot extrusion and spark plasma sintering for producing carbon nanotube reinforced aluminum matrix composites. *Carbon,* 47**,** 570-577.
LEE, J. & FENVES, G. L. 1998. Plastic-damage model for cyclic loading of concrete structures. *Journal of engineering mechanics,* 124**,** 892-900.

LI, C. Y., CHEN, S. J., LU, Y. & DUAN, W. H. Molecular Dynamics Simulations of Graphene Pull-Out from Calcium Silicate Hydrate. International Conference on Mechanics and Physics of Creep, Shrinkage, and Durability of Concrete and Concrete Structures (Christian Hellmich, Johann Kollegger and Bernhard Pichler 21 September 2015 to 23 September 2015), 2015. American Society of Civil Engineers, 913-918.

LI, G. Y., WANG, P. M. & ZHAO, X. 2005. Mechanical behavior and microstructure of cement composites incorporating surface-treated multi-walled carbon nanotubes. *Carbon,* 43**,** 1239-1245.

LI, Q., LU, Y. & MENG, H. 2009. Further investigation on the dynamic compressive strength enhancement of concrete-like materials based on split Hopkinson pressure bar tests. Part II: numerical simulations. *International Journal of Impact Engineering,* 36**,** 1335-1345.

LI, Q. & MENG, H. 2003. About the dynamic strength enhancement of concrete-like materials in a split Hopkinson pressure bar test. *International Journal of Solids and Structures,* 40**,** 343-360.

LI, V. C., STANG, H. & KRENCHEL, H. 1993. Micromechanics of crack bridging in fibre-reinforced concrete. *Materials and structures,* 26**,** 486-494.

LI, V. C., WANG, Y. & BACKER, S. 1991. A micromechanical model of tension-softening and bridging toughening of short random fiber reinforced brittle matrix composites. *Journal of the Mechanics and Physics of Solids,* 39**,** 607-625.

LI, X. Y., KOREYAM, A. H., LI, C. Y., LIU, Y. M., HE, H. S., SANJAYAN, J. G. & DUAN, W. H. 2016a. Incorporation of graphene oxide and silica fume into cement paste: A study of dispersion and compressive strength. *In submission*.

LI, X. Y., LI, C. Y., LIU, Y. M., CHEN, S. J., WANG, C. M., SANJAYAN, J. G. & DUAN, W. H. Improvement of mechanical properties by incorporating graphene oxide into cement mortar. *Mechanics of Advanced Materials and Structures*.

LI, X. Y., LI, C. Y., LIU, Y. M., WANG, C. M., SANJAYAN, J. G. & DUAN, W. H. 2016b. Improvement of mechanical properties by incorporating graphene oxide into cement mortar. *In submission*.

LIANG, J., HUANG, Y., ZHANG, L., WANG, Y., MA, Y., GUO, T. & CHEN, Y. 2009. Molecular-level dispersion of graphene into poly (vinyl alcohol) and effective reinforcement of their nanocomposites. *Advanced Functional Materials,* 19**,** 2297-2302.

LIAO, K. & LI, S. 2001. Interfacial characteristics of a carbon nanotube–polystyrene composite system. *Applied Physics Letters,* 79**,** 4225-4227.

LIN, Z., KANDA, T. & LI, V. C. 1999. On interface property characterization and performance of fiber reinforced cementitious composites. *Concrete Science and Engineering,* 1**,** 173-184.

LIU, F., HU, N., NING, H., LIU, Y., LI, Y. & WU, L. 2015. Molecular dynamics simulation on interfacial mechanical properties of polymer nanocomposites with wrinkled graphene. *Computational Materials Science,* 108, Part A**,** 160-167.

LUBLINER, J., OLIVER, J., OLLER, S. & ONATE, E. 1989. A plastic-damage model for concrete. *International Journal of solids and structures,* 25**,** 299-326.

LV, S., MA, Y., QIU, C., SUN, T., LIU, J. & ZHOU, Q. 2013. Effect of graphene oxide nanosheets of microstructure and mechanical properties of cement composites. *Construction and Building Materials,* 49**,** 121-127.

MALVAR, L. J. & CRAWFORD, J. E. 1998. Dynamic increase factors for concrete. DTIC Document.

MALVAR, L. J. & ROSS, C. A. 1998. Review of strain rate effects for concrete in tension. *Materials Journal,* 95**,** 735-739.

MEHTA, P. K. 1986. Concrete. Structure, properties and materials.

MITTAL, G., DHAND, V., RHEE, K. Y., PARK, S.-J. & LEE, W. R. 2015. A review on carbon nanotubes and graphene as fillers in reinforced polymer nanocomposites. *Journal of Industrial and Engineering Chemistry,* 21**,** 11-25.

MO, Y., TURNER, K. T. & SZLUFARSKA, I. 2009. Friction laws at the nanoscale. *Nature,* 457**,** 1116-1119.

MOON, J., YOON, S. & MONTEIRO, P. J. 2015. Mechanical properties of jennite: A theoretical and experimental study. *Cement and Concrete Research,* 71**,** 106-114.

NAAMAN, A. E. & SHAH, S. P. 1976. Pull-out mechanism in steel fiber-reinforced concrete. *Journal of the Structural Division,* 102**,** 1537-1548.

NEMAT-NASSER, S. 2000. Introduction to high strain rate testing. *ASM handbook,* 8**,** 427-428.

NEMAT-NASSER, S. & DENG, H. 1994. Strain-rate effect on brittle failure in compression. *Acta metallurgica et materialia,* 42**,** 1013-1024.

NEVILLE, A. M. & BROOKS, J. J. 1987. *Concrete technology*.

OŽBOLT, J. & REINHARDT, H. 2002. Numerical study of mixed-mode fracture in concrete. *International journal of fracture,* 118**,** 145-162.

PAN, Z., DUAN, W., LI, D. & COLLINS, F. 2013. Graphene oxide reinforced cement and concrete. Google Patents.

PAN, Z., HE, L., QIU, L., KORAYEM, A. H., LI, G., ZHU, J. W., COLLINS, F., LI, D., DUAN, W. H. & WANG, M. C. 2015. Mechanical properties and microstructure of a graphene oxide–cement composite. *Cement and Concrete Composites,* 58**,** 140-147.

PORWAL, H., TATARKO, P., GRASSO, S., KHALIQ, J., DLOUHÝ, I. & REECE, M. J. 2013. Graphene reinforced alumina nano-composites. *Carbon,* 64**,** 359-369.

QIAN, D., DICKEY, E. C., ANDREWS, R. & RANTELL, T. 2000. Load transfer and deformation mechanisms in carbon nanotube-polystyrene composites. *Applied physics letters,* 76**,** 2868-2870.

QIU, L., YANG, X., GOU, X., YANG, W., MA, Z. F., WALLACE, G. G. & LI, D. 2010a. Dispersing carbon nanotubes with graphene oxide in water and synergistic effects between graphene derivatives. *Chemistry-A European Journal,* 16**,** 10653-10658.

QIU, L., YANG, X., GOU, X., YANG, W., MA, Z. F., WALLACE, G. G. & LI, D. 2010b. Dispersing carbon nanotubes with graphene oxide in water and synergistic effects between graphene derivatives. *Chemistry–A European Journal,* 16**,** 10653-10658.

RIGBY, D., SUN, H. & EICHINGER, B. 1997. Computer simulations of poly (ethylene oxide): force field, PVT diagram and cyclization behaviour. *Polymer International,* 44**,** 311-330.

ROSS, C. A., THOMPSON, P. & TEDESCO, J. 1989. Split-Hopkinson pressure-bar tests on concrete and mortar in tension and compression. *ACI Materials Journal,* 86**,** 475-481.

ROSSI, P. 1991. A physical phenomenon which can explain the mechanical behaviour of concrete under high strain rates. *Materials and Structures,* 24**,** 422-424.

ROSSI, P. & TOUTLEMONDE, F. 1996. Effect of loading rate on the tensile behaviour of concrete: description of the physical mechanisms. *Materials and structures,* 29**,** 116-118.

SAMAL, S. S. & BAL, S. 2008. Carbon nanotube reinforced ceramic matrix composites-a review. *Journal of Minerals and Materials Characterization and Engineering,* 7**,** 355.

SANCHEZ, F. & SOBOLEV, K. 2010. Nanotechnology in concrete–a review. *Construction and Building Materials,* 24**,** 2060-2071.

SHAHSAVARI, R., BUEHLER, M. J., PELLENQ, R. J. M. & ULM, F. J. 2009. First-principles study of elastic constants and interlayer interactions of complex hydrated oxides: Case study of tobermorite and jennite. *Journal of the American Ceramic Society,* 92**,** 2323-2330.

SHIN, S., CHOI, H., SHIN, J. & BAE, D. 2015. Strengthening behavior of few-layered graphene/aluminum composites. *Carbon,* 82**,** 143-151.
SINGH, L., KARADE, S., BHATTACHARYYA, S., YOUSUF, M. & AHALAWAT, S. 2013. Beneficial role of nanosilica in cement based materials–A review. *Construction and Building Materials,* 47**,** 1069-1077.
STANKOVICH, S., DIKIN, D. A., DOMMETT, G. H., KOHLHAAS, K. M., ZIMNEY, E. J., STACH, E. A., PINER, R. D., NGUYEN, S. T. & RUOFF, R. S. 2006a. Graphene-based composite materials. *nature,* 442**,** 282-286.
STANKOVICH, S., PINER, R. D., CHEN, X., WU, N., NGUYEN, S. T. & RUOFF, R. S. 2006b. Stable aqueous dispersions of graphitic nanoplatelets via the reduction of exfoliated graphite oxide in the presence of poly (sodium 4-styrenesulfonate). *Journal of Materials Chemistry,* 16**,** 155-158.
SUN, H. 1998. COMPASS: an ab initio force-field optimized for condensed-phase applications overview with details on alkane and benzene compounds. *The Journal of Physical Chemistry B,* 102**,** 7338-7364.
SUNG, N.-H. & SUH, N. P. 1979. Effect of fiber orientation on friction and wear of fiber reinforced polymeric composites. *Wear,* 53**,** 129-141.
TANG, L.-C., WAN, Y.-J., YAN, D., PEI, Y.-B., ZHAO, L., LI, Y.-B., WU, L.-B., JIANG, J.-X. & LAI, G.-Q. 2013. The effect of graphene dispersion on the mechanical properties of graphene/epoxy composites. *Carbon,* 60**,** 16-27.
TEDESCO, J., HUGHES, M. & ROSS, C. 1994. Numerical simulation of high strain rate concrete compression tests. *Computers & structures,* 51**,** 65-77.
TEDESCO, J. W. & ROSS, C. A. 1993. Experimental and numerical analysis of high strain rate splitting-tensile tests. *ACI Materials journal,* 90.
TEDESCO, J. W., ROSS, C. A. & KUENNEN, S. T. 1993. Experimental and numerical analysis of high strain rate splitting tensile tests. *ACI Materials journal,* 90**,** 162-162.
TRAN, T. K. & KIM, D. J. 2014. High strain rate effects on direct tensile behavior of high performance fiber reinforced cementitious composites. *Cement and Concrete Composites,* 45**,** 186-200.
TSUDA, T., OGASAWARA, T., DENG, F. & TAKEDA, N. 2011. Direct measurements of interfacial shear strength of multi-walled carbon nanotube/PEEK composite using a nano-pullout method. *Composites Science and Technology,* 71**,** 1295-1300.
WALKER, L. S., MAROTTO, V. R., RAFIEE, M. A., KORATKAR, N. & CORRAL, E. L. 2011. Toughening in graphene ceramic composites. *Acs Nano,* 5**,** 3182-3190.
WANG, J., LI, Z., FAN, G., PAN, H., CHEN, Z. & ZHANG, D. 2012a. Reinforcement with graphene nanosheets in aluminum matrix composites. *Scripta Materialia,* 66**,** 594-597.
WANG, Q., DUAN, W., LIEW, K. & HE, X. 2007. Inelastic buckling of carbon nanotubes. *Applied physics letters,* 90**,** 033110.
WANG, S., ZHANG, M.-H. & QUEK, S. T. 2012b. Mechanical behavior of fiber-reinforced high-strength concrete subjected to high strain-rate compressive loading. *Construction and Building Materials,* 31**,** 1-11.
WICHMANN, M. H., SCHULTE, K. & WAGNER, H. D. 2008. On nanocomposite toughness. *Composites Science and Technology,* 68**,** 329-331.
WU, C. & XU, W. 2006. Atomistic molecular modelling of crosslinked epoxy resin. *Polymer,* 47**,** 6004-6009.
WU, W., ZHANG, W. & MA, G. 2010. Mechanical properties of copper slag reinforced concrete under dynamic compression. *Construction and building materials,* 24**,** 910-917.
XIA, Z. & CURTIN, W. 2004. Pullout forces and friction in multiwall carbon nanotubes. *Physical Review B,* 69**,** 233408.

XIA, Z., RIESTER, L., CURTIN, W., LI, H., SHELDON, B., LIANG, J., CHANG, B. & XU, J. 2004. Direct observation of toughening mechanisms in carbon nanotube ceramic matrix composites. *Acta Materialia,* 52**,** 931-944.

XU, Y., HONG, W., BAI, H., LI, C. & SHI, G. 2009. Strong and ductile poly (vinyl alcohol)/graphene oxide composite films with a layered structure. *Carbon,* 47**,** 3538-3543.

XU, Z. & GAO, C. 2010. In situ polymerization approach to graphene-reinforced nylon-6 composites. *Macromolecules,* 43**,** 6716-6723.

ZHANDAROV, S. & MÄDER, E. 2005. Characterization of fiber/matrix interface strength: applicability of different tests, approaches and parameters. *Composites Science and Technology,* 65**,** 149-160.

ZHANG, M., WU, H., LI, Q. & HUANG, F. 2009. Further investigation on the dynamic compressive strength enhancement of concrete-like materials based on split Hopkinson pressure bar tests. Part I: Experiments. *International journal of impact engineering,* 36**,** 1327-1334.

ZHOU, X. & HAO, H. 2008. Modelling of compressive behaviour of concrete-like materials at high strain rate. *International Journal of Solids and Structures,* 45**,** 4648-4661.

ZHU, Y., MURALI, S., CAI, W., LI, X., SUK, J. W., POTTS, J. R. & RUOFF, R. S. 2010. Graphene and graphene oxide: synthesis, properties, and applications. *Advanced materials,* 22**,** 3906-3924.

ZOU, B., CHEN, S. J., KORAYEM, A. H., COLLINS, F., WANG, C. & DUAN, W. H. 2015. Effect of ultrasonication energy on engineering properties of carbon nanotube reinforced cement pastes. *Carbon,* 85**,** 212-220.

ZUO, P.-P., FENG, H.-F., XU, Z.-Z., ZHANG, L.-F., ZHANG, Y.-L., XIA, W. & ZHANG, W.-Q. 2013. Fabrication of biocompatible and mechanically reinforced graphene oxide-chitosan nanocomposite films. *Chem Cent J,* 7**,** 39-39.